

# ***SatFusion: A Unified Framework for Enhancing Remote Sensing Image via Multi-Frame and Multi-Source Image Fusion***

**Yufei Tong · Guanjie Cheng · Peihan Wu · Feiyi Chen · Xinkui Zhao ·  
Shuiguang Deng**

Received: date / Accepted: date

**Abstract** Remote sensing (RS) imaging is constrained by hardware cost and physical limitations, making high-quality image acquisition challenging and motivating the use of image fusion for quality enhancement. Multi-Frame Super-Resolution (MFSR) and Pansharpening exploit complementary information from multiple frames and multiple sources, respectively, but are typically studied in isolation: MFSR lacks high-resolution structural priors for fine-grained texture recovery, while Pansharpening relies on upsampling low-resolution multispectral images and is therefore sensitive to noise and misalignment. With the rapid development of the Satellite Internet of Things (Sat-IoT), collaboratively leveraging large numbers of low-quality yet information-complementary images has become a central challenge.

To address this challenge, we propose ***SatFusion***, a unified framework for enhancing RS image via multi-

Guanjie Cheng is the corresponding author.

Yufei Tong  
Zhejiang University, Hangzhou, China  
E-mail: yufeitong@zju.edu.cn

Guanjie Cheng  
Zhejiang University, Hangzhou, China  
E-mail: chengguanjie@zju.edu.cn

Peihan Wu  
Zhejiang University, Hangzhou, China  
E-mail: 22321313@zju.edu.cn

Feiyi Chen  
Zhejiang University, Hangzhou, China  
E-mail: chenfeiyi@zju.edu.cn

Xinkui Zhao  
Zhejiang University, Hangzhou, China  
E-mail: zhaoxinkui@zju.edu.cn

Shuiguang Deng  
Zhejiang University, Hangzhou, China  
E-mail: dengsg@zju.edu.cn

frame and multi-source image fusion. ***SatFusion*** employs a Multi-Frame Image Fusion (MFIF) module to extract high-resolution semantic features from multiple low-resolution multispectral frames, and incorporates fine-grained structural information from a high-resolution panchromatic image through a Multi-Source Image Fusion (MSIF) module, enabling robust feature integration with implicit pixel-level alignment. To further alleviate the lack of structural priors in multi-frame fusion, we introduce ***SatFusion***<sup>\*</sup>, which integrates a panchromatic-guided mechanism into the multi-frame fusion stage. Through structure-aware feature embedding and transformer-based adaptive aggregation, ***SatFusion***<sup>\*</sup> enables spatially adaptive selection of multi-frame features, strengthening the coupling between multi-frame and multi-source representations. Extensive experiments on the WorldStrat, WV3, QB, and GF2 datasets demonstrate that our methods significantly outperform existing methods in terms of reconstruction quality, robustness, and generalizability.

**Keywords** Remote Sensing, Image Fusion, Pansharpening, Multi-Frame Super-Resolution, Sat-IoT

## 1 Introduction

Image fusion aims to reconstruct a high-quality image by integrating complementary information from multiple low-quality images, offering an effective solution to the hardware constraints. Remote sensing (RS) imagery is indispensable for applications such as environmental monitoring, defense intelligence, and urban planning [10, 23, 34, 50, 53, 55, 56]. In practice, sensors acquire either high-resolution images with limited spectral content or low-resolution images with rich spectral information [28, 36]. Furthermore, the rapid expansion of

the Satellite Internet of Things (Sat-IoT) [20, 21, 27, 44] has led to an explosive growth of multi-frame and multi-source image data, placing increasing demands on fusion algorithms to efficiently leverage large-scale, low-quality yet complementary images.

In the RS domain, image fusion has been primarily studied along two major directions: Multi-Frame Super-Resolution (MFSR) and Pansharpening. MFSR [2, 3, 7, 8, 38, 48] aims to reconstruct a high-resolution image by exploiting complementary information from multi-frame low-resolution images acquired by the same type of sensor over the same scene. Owing to platform motion, attitude variations, and orbital differences, these images provide diverse low-resolution samplings of the underlying scene, which can be effectively leveraged for resolution enhancement. With the rapid expansion of low-cost satellite systems, where imaging resolution is often limited, MFSR has emerged as a key technique for enabling cost-effective high-quality image reconstruction. In contrast, Pansharpening [6, 16, 17, 28, 32, 40, 42, 60] focuses on fusing multi-source images from different types of sensors over the same scene. Specifically, it combines a high-resolution panchromatic (PAN) image with a low-resolution multispectral (MS) image exploiting complementary spatial and spectral information to produce a high-resolution MS image.

Despite their respective advantages, both MFSR and Pansharpening face several fundamental challenges. First, MFSR operates on multi-frame low-resolution images acquired by homogeneous sensors. Although these images contain complementary spatial information, the lack of high-resolution structural priors limits the recovery of fine-grained textures, leading to a performance bottleneck. As shown in Fig. 1, images reconstructed by MFSR are generally of lower quality than those produced by Pansharpening. Second, Pansharpening relies on multi-source images but is highly sensitive to input quality and inter-source misalignment caused by differences in sensor positions, acquisition times, and imaging conditions. As shown in Fig. 2(b), since the spatial resolution of a PAN image is typically several times higher than that of an MS image, the MS image must be first upsampled to the PAN resolution to enable pixel-wise spatial alignment prior to fusion [5, 9, 14, 30, 45, 46, 51, 54, 59]. However, this upsampling step inevitably introduces interpolation artifacts and spatial shifts, which further exacerbate inter-image misalignment. Moreover, as illustrated in Fig. 1, the performance of Pansharpening is heavily dependent on the quality of the MS image, because the upsampling process amplifies noise perturbations, leading to pronounced degradation in fusion quality. Most existing Pansharpening assumes clean inputs and perfect pixel-level alignment and rely heavily

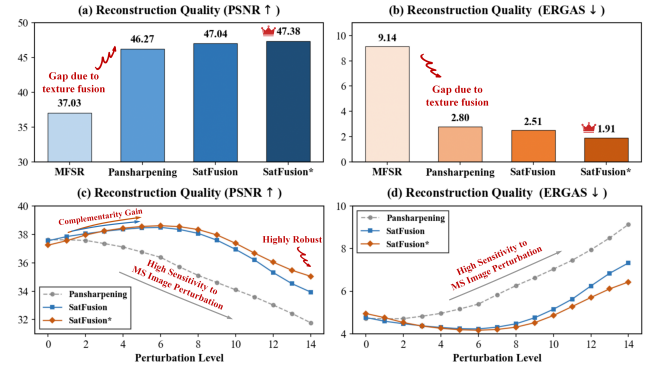


Fig. 1: (a-b) Reconstruction quality across different methods on the WorldStrat dataset. The significant performance gap between MFSR and Pansharpening highlights the necessity of incorporating fine-grained spatial textures from PAN images. (c-d) PSNR and ERGAS under 15 increasing perturbation levels on the QB dataset. Each level corresponds to a predefined combination of blur, misalignment, and noise applied to the MS image, with higher levels indicating more severe perturbations. While traditional Pansharpening suffers from a steep performance collapse as perturbation intensifies, our proposed *SatFusion* and *SatFusion\** maintain superior robustness, effectively mitigating input artifacts through multi-frame complementary information.

on pixel-wise reconstruction losses, which often result in severe blurring artifacts when noise and misalignment are present [9]. Third, sensors continuously generate increasing volumes of multi-frame and multi-source images for the same scene. Existing MFSR and Pansharpening are unable to jointly process such images in a unified framework.

To address these challenges, we propose *SatFusion*, which reconstructs high-resolution MS image by simultaneously exploiting complementary information from multiple low-resolution MS images and a high-resolution PAN image. The framework consists of three components: a Multi-Frame Image Fusion (MFIF) module, a Multi-Source Image Fusion (MSIF) module, and a Fusion Composition module. Unlike conventional Pansharpening that assume clean inputs and perfect pixel-level alignment and rely on upsampling low-resolution MS image to explicitly match the PAN resolution, *SatFusion* achieves implicitly spatial alignment by MFIF module which extracts and fuses features from multiple MS frames to produce high-resolution deep semantic features. In contrast to conventional MFSR, *SatFusion* explicitly injects fine-grained structural priors by MSIF module, substantially improving spatial detail reconstruction. The Fusion Composition module adaptively integrates multi-frame and multi-source features, where

the reconstruction is supervised by a weighted combination of different loss functions. Importantly, the MFIF and MSIF modules are designed with unified feature representations and standardized fusion interfaces, endowing *SatFusion* with strong extensibility and flexibility. This design allows a wide range of existing MFSR and Pansharpening methods to be naturally embedded into the framework without substantial architectural modifications. *SatFusion* serves as a unified framework that breaks the traditional paradigm of treating multi-frame and multi-source fusion independently. As illustrated in Fig. 1, through end-to-end optimization, it achieves systematic performance improvements, enabling higher-quality and more robust RS image reconstruction.

Although *SatFusion* significantly advances image fusion, its MFIF module does not fully exploit the structural priors provided by PAN image during multi-frame fusion stage. Local misalignment and noise exist among multi-frame MS images, primarily caused by variations in acquisition time, viewing angles, and environmental conditions. In contrast, PAN images offer stable geometric structures. We further propose *SatFusion*\*, which incorporates PAN guidance into the MFIF module. Specifically, the PAN image is first downsampled and concatenated with multi-frame MS features along the channel dimension before being fed into the MFIF encoder. Furthermore, we optimize the transformer-based fusion module within MFIF module by leveraging PAN-guided features to generate position-dependent fusion references. Through attention mechanisms, these references guide the adaptive aggregation of multi-frame features, allowing structural constraints provided by the PAN image to directly participate in multi-frame fusion decisions. As shown in Fig. 1, *SatFusion*\* further improves fusion quality and robustness. In addition, *SatFusion*\* supports an arbitrary number of input frames and maintains strong performance when the number of input images differs from that used during training.

The contributions of this work are as follows:

1. We reveal the inherent structural complementarity between MFSR and Pansharpening and propose ***SatFusion***, the first unified framework for enhancing RS image via multi-frame and multi-source image fusion. To the best of our knowledge, this is the first work to investigate the joint optimization of multi-frame and multi-source RS images within a unified framework.
2. We further propose ***SatFusion*\***. By incorporating structural priors into the MFIF module, *SatFusion*\* enables spatially adaptive multi-frame feature aggregation, strengthening the coupling between multi-frame and multi-source features and improving model generalization across diverse input scenarios.

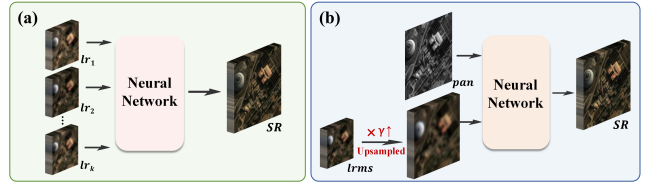


Fig. 2: (a) The schematic diagram of MFSR. (b) The schematic diagram of Pansharpening.

3. Comprehensive experiments on the WorldStrat, WV3, QB, and GF2 datasets demonstrate the superiority of *SatFusion* in terms of reconstruction quality and robustness, as well as the further improvements achieved by *SatFusion*\*.
4. By effectively bridging the gap between low-quality redundant data and users' demand for high-quality imagery, our framework offers an efficient and deployable solution for RS scenarios.

The remainder of this paper is organized as follows. Sec. 2 reviews related work and motivations. Sec. 3 introduces the proposed *SatFusion* and *SatFusion*\*. Sec. 4 introduces datasets, training and evaluation protocols. Sec. 5 provides detailed experimental analyses. Sec. 6 discusses the effectiveness and implications of *SatFusion* and *SatFusion*\*. Finally, Sec. 7 concludes this work.

## 2 Related Work and Motivations

Depending on the type of input images, RS image fusion can be broadly categorized into two directions: Multi-Frame Super-Resolution (MFSR) and Pansharpening. In this section, we review these two paradigms and motivate our study through experimental observations.

### 2.1 Multi-Frame Super-Resolution

MFSR aims to extract information from multi-frame low-resolution images of the same scene to reconstruct a high-resolution image. Extensive studies have shown that, compared to Single-Frame Super-Resolution (SFSR), which relies solely on image priors, MFSR effectively fuses additional data to produce more reliable reconstructions [2, 3, 7, 8, 33, 38]. As illustrated in Fig. 2(a), the image reconstruction task in an MFSR network can be formulated as:

$$SR = f_{MFSR}(\{lr_i\}_{i=1}^k), \quad (1)$$

where the input set  $\{lr_i\}_{i=1}^k \in \mathbb{R}^{k \times H \times W \times C}$  denotes  $k$  low-resolution images, and the output  $SR \in \mathbb{R}^{\gamma H \times \gamma W \times C}$

represents the fused high-resolution image. Here,  $\gamma$  denotes the spatial upscaling factor, while  $k$ ,  $C$ ,  $H$ , and  $W$  represent the number of images, channels, height, and width, respectively. The output  $SR$  maintains the same number of channels and is enlarged by a factor of  $\gamma$  in the spatial dimensions.

With the increasing availability of multiple images for the same scene, MFSR has attracted significant research interest. For instance, in photography, a typical approach is Burst Image Super-Resolution, which reconstructs a high-resolution image by fusing multiple similar but slightly misaligned low-resolution frames. Bhat et al. [3] developed BurstSR, an MFSR network for handheld cameras that uses pixel-level optical flow for alignment and attention-based feature fusion. Wei et al. [48] proposed the Federated Burst Affinity Network, which effectively aggregates multi-frame information through geometric alignment and a federated affinity fusion strategy, assisted by Transformer-based representation learning. Di et al. [8] introduced an MFSR model based on a Query State Space Model, explicitly modeling the sub-pixel consistency distribution in multi-frame images and designing an adaptive upsampling module to enhance detail reconstruction.

In RS imagery, multi-frame images are typically captured by the same type of sensor, therefore share similar spectral characteristics. The MFSR task is often referred to as Multi-Image Super-Resolution (MISR), and most studies treat MFSR and MISR interchangeably. In this paper, we follow the same convention. Multi-Frame SR-CNN [4] concatenates multi-frame features along the channel dimension and fuses them using 2D convolutions. HighRes-Net [7,37] is an end-to-end MFSR network that first encodes  $\{LR_i\}_{i=1}^k$  and then recursively fuses multi-frame features with 2D convolutions over  $t = \log_2 k$  steps. DeepSUM [33] uses 3D convolutions to integrate across channels, achieving feature-level alignment and fusion. Its fusion module also employs a recursive structure, requiring  $k/2$  3D convolution layers to merge  $k$  registered frames. RAMS [38] introduces Residual Temporal Attention Blocks with 2D convolutions and Residual Feature Attention Blocks with 3D convolutions to maximize feature retention along both temporal and spatial dimensions. TR-MISR [2] proposes a transformer-based end-to-end network capable of fusing an arbitrary number of input images. Features corresponding to the same region across multiple frames are fused using an additional learnable embedding vector consistent across the spatial dimension, allowing each output region to simultaneously observe all corresponding input regions.

## 2.2 Pansharpening

Pansharpening aims to fuse multi-source observations of the same scene, specifically a high-resolution PAN image and a low-resolution MS image acquired by different sensor modalities, to generate a high-resolution MS image. As illustrated in Fig. 2(b), the image reconstruction task in a Pansharpening network can be formulated as:

$$SR = f_{Pansharpening}(lrms, pan), \quad (2)$$

where  $lrms \in \mathbb{R}^{H \times W \times C}$  denotes the low-resolution MS image,  $pan \in \mathbb{R}^{\gamma H \times \gamma W \times 1}$  denotes the high-resolution PAN image which provides a stable and fine-grained structural prior, and the output  $SR \in \mathbb{R}^{\gamma H \times \gamma W \times C}$  represents the fused high-resolution MS image. Here,  $\gamma$  denotes the spatial upscaling factor, while  $C$ ,  $H$ , and  $W$  denote the number of MS spectral channels, height, and width, respectively. The output  $SR$  preserves the spectral channels of the MS image while matching the resolution of the PAN image.

Due to the resolution discrepancy between MS and PAN inputs, the MS image is typically upsampled to align with the PAN image prior to fusion. In recent years, a wide range of deep learning-based methods have been proposed to improve performance. A seminal work is PNN [30], which employed a three-layer convolutional network and achieved state-of-the-art performance at the time. Since then, convolutional neural network (CNN)-based approaches have driven substantial progress in Pansharpening, including PanNet [54], DiCNN [14], FusionNet [5], and U2Net [35]. More recently, diffusion-based methods [19, 31, 51, 52, 59] have been introduced, leveraging iterative denoising processes to improve reconstruction quality. Although diffusion models can achieve superior performance, their high computational cost limits their practicality in real-world applications. Furthermore, spatial state-space models and adaptive convolution mechanisms [12, 18, 45] have also been explored for Pansharpening. Pan-Mamba [15] exploits the efficient long-range dependency modeling capability of Mamba to recover fine MS details, while ARConv [45] introduces learnable non-square convolution kernels to adaptively adjust receptive field shapes, enabling more effective capture of anisotropic structural patterns commonly observed in RS imagery.

## 2.3 Motivations

RS satellite imaging scenarios impose more stringent requirements on both MFSR and Pansharpening. For the MFSR, first, unlike burst photography scenarios where frames exhibit strong correlations and small parallax,

satellite multi-frame images are often acquired with relatively long temporal intervals. As a result, inter-frame correlations are weaker, and variations caused by orbital changes and environmental factors introduce additional noise, which significantly limits reconstruction quality. Second, the number of images available for the same scene is inherently variable, requiring MFSR to generalize well to different numbers of input frames, especially when the number of frames during testing differs from that seen during training. However, this issue has received limited attention in existing MFSR studies. For Pansharpening, real-world satellite imaging conditions often lead to noise contamination and spatial misalignment between MS and PAN images. However, most existing Pansharpening assumes clean inputs and perfect pixel-level alignment, which rarely hold in practical scenarios.

As illustrated in Fig. 1, our experiments reveal two key observations: images reconstructed by MFSR are generally of noticeably lower quality than those produced by Pansharpening, while the performance of Pansharpening is highly sensitive to the quality of the low-resolution MS image. We analyze the underlying causes from the fundamental characteristics of the two tasks. On the one hand, MFSR operates on multiple low-resolution images acquired by homogeneous sensors. Although these images contain complementary spatial information, the lack of fine-grained texture details from high-resolution imagery creates an inherent bottleneck for further performance improvement. On the other hand, Pansharpening involves a spatial resolution discrepancy between MS and PAN inputs, necessitating upsampling of the MS image prior to fusion. This upsampling process introduces interpolation artifacts and spatial shifts, which further amplify inter-image misalignment. Moreover, upsampling also magnifies noise perturbations in the MS image, leading to a significant degradation in fusion quality.

To address these issues, we propose *SatFusion*. By incorporating fine-grained texture information from PAN image, *SatFusion* substantially enhances the fusion capability of MFSR. Meanwhile, by fusing multiple low-resolution MS images to generate high-resolution deep semantic features, *SatFusion* achieves implicit pixel-level alignment with PAN image without relying on direct MS upsampling, thereby improving the robustness and effectiveness of Pansharpening. Furthermore, we introduce *SatFusion\**, which strengthens the coupling between multi-frame and multi-source features. Experimental results demonstrate that *SatFusion\** achieves further improvements in fusion quality, robustness to input image degradation, and generalization across varying numbers of input images.

### 3 The Approach

In this section, we first present the problem formulation of multi-frame and multi-source RS image fusion, then introduce the detailed designs of the proposed *SatFusion*, *SatFusion\** frameworks and the loss function.

#### 3.1 Problem Formulation

Based on the motivations discussed in Sec. 2.3, we formulate a new problem that better matches real-world scenarios: reconstructing a high-quality high-resolution MS image by jointly fusing multiple low-quality multi-frame MS images and a PAN image of the same scene. The task is defined as:

$$SR = f(\{lrms_i\}_{i=1}^k, pan), \quad (3)$$

Here,  $\{lrms_i\}_{i=1}^k \in \mathbb{R}^{k \times H \times W \times C}$  denotes a set of  $k$  low-resolution MS images, and  $pan \in \mathbb{R}^{\gamma H \times \gamma W \times 1}$  represents the high-resolution PAN image. The output  $SR \in \mathbb{R}^{\gamma H \times \gamma W \times C}$  represents the reconstructed high-resolution MS image. The factor  $\gamma$  denotes the spatial upscaling factor,  $C$  is the number of MS spectral channels, and  $k$ ,  $H$ , and  $W$  denote the number of input images, height, and width, respectively. The output image  $SR$  preserves the channels of the MS images while preserving the resolution of the PAN image.

#### 3.2 *SatFusion*

*SatFusion* is designed to achieve the following objectives: (1) to construct a unified framework that jointly fuses multi-frame and multi-source images, exploiting their complementary information to improve reconstruction quality; (2) to maintain robustness under challenging conditions such as noise perturbations and inter-image misalignment; (3) to ensure scalability, such that existing MFSR and Pansharpening can be naturally embedded into the framework without substantial architectural modifications, thereby improving both performance and robustness.

Given  $\{lrms_i\}_{i=1}^k$  and  $pan$  as inputs, *SatFusion* outputs the high-resolution MS image  $SR$ . As illustrated in Fig. 3, *SatFusion* consists of three components: a Multi-Frame Image Fusion (MFIF) module, a Multi-Source Image Fusion (MSIF) module, and a Fusion Composition module. We describe these modules in detail below:

**(1) MFIF Module:** The MFIF module aims to fuse information from  $\{lrms_i\}_{i=1}^k$  and generate high-resolution deep semantic features  $SR^{MFIF} \in \mathbb{R}^{\gamma H \times \gamma W \times C}$ ,

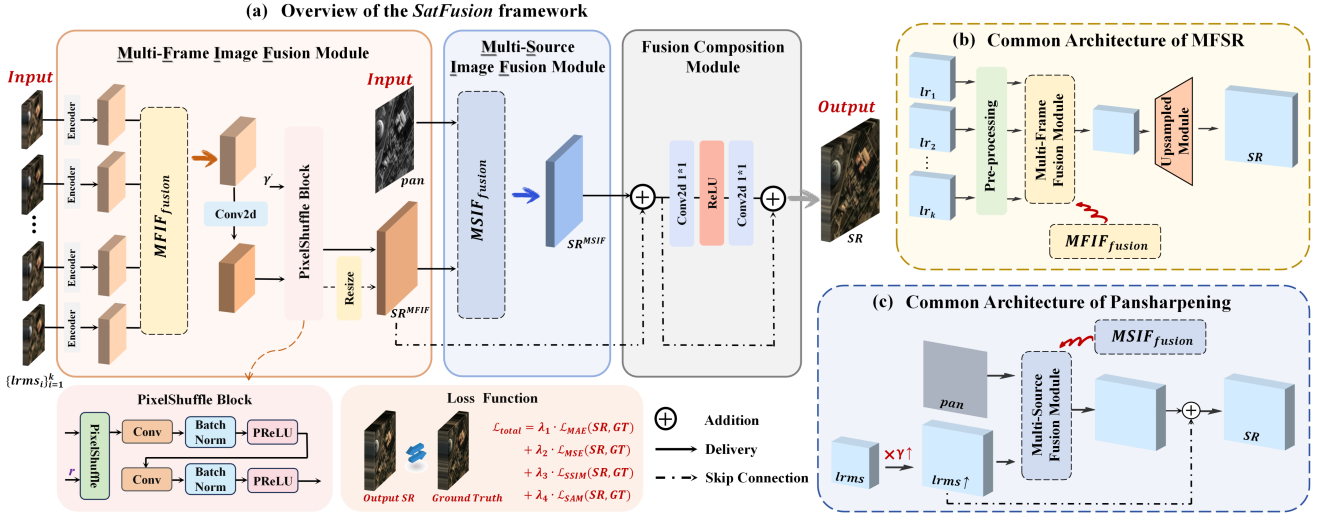


Fig. 3: (a) Overview of the *SatFusion* framework. The MFIF module extracts complementary information from  $\{lrms_i\}_{i=1}^k$  and produces multi-frame fusion features  $SR^{MFIF}$  that are spatially aligned with *pan* resolution. The MSIF module injects fine-grained texture details from *pan* to generate multi-source fusion features  $SR^{MSIF}$ . The Fusion Composition module further integrates complementary advantages across features, while the reconstruction is jointly supervised by a weighted combination of different loss functions. (b-c) Common architecture of MFSR and PanSharpening. Existing fusion components from MFSR and PanSharpening methods can be naturally embedded into the *SatFusion* framework.

thereby achieving implicit pixel-level spatial alignment with *pan*. This process can be formulated as:

$$SR^{MFIF} = MFIF(\{lrms_i\}_{i=1}^k). \quad (4)$$

The MFIF module consists of three components: an encoder denoted as  $MFIF_{encode}(\cdot)$ , a multi-frame fusion module denoted as  $MFIF_{fusion}(\cdot)$ , and a decoder denoted as  $MFIF_{decode}(\cdot)$ . First, each input MS image is passed through a shared-weight convolution(conv) encoder to extract features. Then, these features are fused by fusion module. The fused feature is then decoded into high-resolution deep semantic feature:

$$\begin{aligned} \{x_i^{encode}\}_{i=1}^k &= MFIF_{encode}(\{lrms_i\}_{i=1}^k), \\ x^{fusion} &= MFIF_{fusion}(\{x_i^{encode}\}_{i=1}^k), \\ SR^{MFIF} &= MFIF_{decode}(x^{fusion}), \end{aligned} \quad (5)$$

where  $\{x_i^{encode}\}_{i=1}^k \in \mathbb{R}^{k \times H \times W \times C_{encode}}$  denotes the encoded features,  $x^{fusion} \in \mathbb{R}^{H \times W \times C_{fusion}}$  represents the fused feature map.

As shown in Fig. 3(b), in existing MFSR methods [2, 4, 7, 33, 38], the fusion of multi-frame features is a crucial step that precedes the upsampling module for reconstructing high-resolution outputs. As discussed in Sec. 2.1, representative approaches include 2D, 3D conv, and transformer-based fusion strategies. As a unified framework, *SatFusion* can adopt any of these methods

as  $MFIF_{fusion}$ , enabling the multi-frame fusion modules existing in MFSR to be naturally integrated into *SatFusion*, as shown in Fig. 3(a).

$MFIF_{decode}$  adjusts the resolution to align with *pan* and the channel dimension to match the ground-truth(GT). We implement the decoder using a sub-pixel conv block named PixelShuffle Block, sub-pixel conv [39] increases the resolution of feature maps by rearranging the channel dimension into the spatial dimension:

$$x^{decode} = PSBlock(Conv2d(x^{fusion}), \gamma'), \quad (6)$$

where  $PSBlock$  denotes the PixelShuffle Block,  $x^{decode} \in \mathbb{R}^{\gamma' H \times \gamma' W \times C}$  is the output feature map, and  $\gamma'$  denotes the spatial upscaling factor of the sub-pixel conv.  $Conv2d$  adjusts the channel dimension to be divisible by  $\gamma'^2$ , ensuring correct pixel rearrangement.  $PSBlock$  consists of pixel rearrangement followed by stacked 2D conv, batch normalization(BN), and PReLU activation.

Actually, the upscaling factor  $\gamma'$  of the sub-pixel conv is not required to be equal to the final resolution upscaling factor  $\gamma$  of *SR*. That is, when  $\gamma' \neq \gamma$ , the feature map  $x^{decode}$  needs to be further adjusted in order to achieve spatial alignment with *pan*. Accordingly,  $x^{decode}$  is optionally passed through a *Resize* module:

$$SR^{MFIF} = \begin{cases} x^{decode}, & \text{if } \gamma' = \gamma, \\ Resize(x^{decode}), & \text{otherwise,} \end{cases} \quad (7)$$

where  $\text{Resize}(\cdot)$  applies interpolation to ensure spatial alignment with  $pan$ . Unless otherwise specified, we set  $\gamma' = \gamma$  by default.

**(2) MSIF Module:** The MSIF module aims to fuse the deep semantic features  $SR^{MFIF}$  from multi-frame images with the fine-grained texture features of  $pan$ , so as to generate a detail-rich feature map  $SR^{MSIF} \in \mathbb{R}^{\gamma H \times \gamma W \times C}$ , which can be formulated as follows:

$$SR^{MSIF} = MSIF(SR^{MFIF}, pan). \quad (8)$$

The MSIF module consists of a multi-source fusion component called  $MSIF_{fusion}$ :

$$SR^{MSIF} = MSIF_{fusion}(SR^{MFIF}, pan). \quad (9)$$

Due to the task setting, Pansharpening inevitably performs multi-source fusion between  $pan$  and the MS image that has been upsampled via interpolation [5, 15, 30, 35, 45], as shown in Fig. 3(c). Similar to the design philosophy of  $MFIF_{fusion}$ , as a unified framework, *SatFusion* can adopt Pansharpening fusion modules described in Sec. 2.2 as the  $MSIF_{fusion}$ . As illustrated in Fig. 3(a), the multi-source fusion module in Pansharpening can be naturally embedded into *SatFusion*.

**(3) Fusion Composition Module:** The Fusion Composition module adaptively integrates the outputs of the MFIF and MSIF modules to fully exploit the advantages of both multi-frame and multi-source fusion. Given  $SR^{MFIF}$  and  $SR^{MSIF}$  as inputs, the final reconstruction is obtained as

$$SR = \text{Fusion}(SR^{MFIF}, SR^{MSIF}). \quad (10)$$

This module consists of feature aggregation and refinement operation, which ultimately output  $SR$ :

$$\begin{aligned} SR^{res} &= SR^{MFIF} + SR^{MSIF}, \\ SR &= \text{ConvBlock}(SR^{res}) + SR^{res}, \end{aligned} \quad (11)$$

Here,  $SR \in \mathbb{R}^{\gamma H \times \gamma W \times C}$  denotes the final high-resolution MS image.  $\text{ConvBlock}$  consists of stacked  $1 \times 1$  2D conv, which are effective for spectral adjustment [37]. Although formulated in a residual manner, the fusion is not a simple averaging of  $SR^{MFIF}$  and  $SR^{MSIF}$ ; instead, the learned  $1 \times 1$  convolutions perform content-adaptive, pixel-wise spectral re-weighting to selectively integrate complementary information from the two branches.

### 3.3 *SatFusion*\*

The extensibility of *SatFusion* as a unified framework enables existing methods to be seamlessly integrated. However, in *SatFusion*, the MFIF module performs multi-frame fusion without explicit guidance from stable

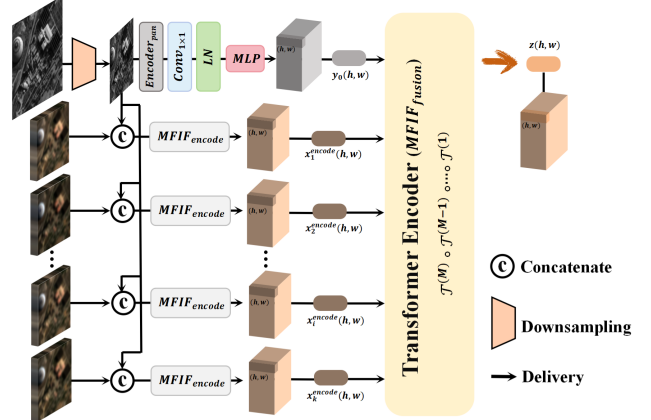


Fig. 4: Architecture of the enhanced MFIF module in *SatFusion*\*. *SatFusion*\* introduces PAN-guided optimization in both  $MFIF_{encode}$  and  $MFIF_{fusion}$ . During encoding, PAN features provide stable structural references to guide multi-frame feature alignment. During fusion, a transformer-based mechanism employs PAN-guided, position-dependent embeddings to adaptively aggregate multi-frame features.

spatial structural information. Although structural cues can be implicitly propagated to the MFIF parameters through back-propagation of reconstruction losses, such indirect supervision may lead to suboptimal fusion under spatial misalignment and noise perturbations. Moreover, existing MFSR methods generally pay limited attention to generalization with respect to the number of input frames, which restricts their applicability when the number of input images during testing differs from that used in training. To address these limitations, we further propose *SatFusion*\*

As shown in Fig. 4, *SatFusion*\* enhances the MFIF module of *SatFusion* by optimizing both  $MFIF_{encode}$  and  $MFIF_{fusion}$ . Specifically,  $pan$ , containing more stable and reliable structural information, serves as a reference. During encoding,  $pan$  features are used to guide alignment, while during fusion, a transformer-based mechanism leverages  $pan$ -guided position-dependent embeddings to adaptively aggregate multi-frame features. We describe  $MFIF_{encode}$  and  $MFIF_{fusion}$  in detail below:

**(1)  $MFIF_{encode}$ :** MFSR assumes that multiple frames jointly contain richer information than a single image. However, variations in environmental conditions across frames often lead to local misalignment and noise. To alleviate this issue, we introduce a *weak geometric anchor* during the encoding stage by incorporating  $pan$  as structural prior.

Specifically,  $pan$  is first downsampled to match the spatial resolution of the MS images, and then concate-

nated ( $\oplus$ ) with each low-resolution MS image along the channel dimension and jointly fed into the shared-weight conv encoder  $MFIF_{encode}$ :

$$\begin{aligned} pan\downarrow &= \text{Downsampling}(pan), \\ x_i^{encode} &= MFIF_{encode}(lrms_i \oplus pan\downarrow), \end{aligned} \quad (12)$$

where  $pan\downarrow \in \mathbb{R}^{H \times W \times 1}$  denotes the downsampled  $pan$ , and  $\{x_i^{encode}\}_{i=1}^k \in \mathbb{R}^{k \times H \times W \times C_{encode}}$  represents the encoded multi-frame features. These features are subsequently fused by  $MFIF_{fusion}$ .

**(2)  $MFIF_{fusion}$ :** Some existing MFSR methods concatenate multi-frame features along the channel dimension and apply conv for fusion [4, 33, 38]. Such designs require the number of input frames during inference to be identical to that during training, resulting in limited generalization. In contrast, transformer architectures naturally support variable-length inputs via self-attention mechanisms [41] and have been widely adopted in image modeling to capture long-range spatial dependencies [11, 13, 22, 25, 26]. In multi-frame fusion, however, the primary objective is to model relationships across frames rather than within a single image. TR-MISR [2] addresses this by focusing on features from the same spatial region across frames and aggregating them using a single global learnable embedding (*CLS token*). Unlike TR-MISR, which relies on a globally shared fusion token, *SatFusion\** introduces *pan-guided, position-specific fusion tokens*, enabling spatially adaptive multi-frame aggregation under stable structural guidance.

Specifically, we first feed the downsampled PAN image  $pan\downarrow$ , obtained in the encoding stage of the MFIF module, into a dedicated PAN encoder  $Encoder_{pan}$  composed of stacked  $3 \times 3$  conv. This encoder extracts structural features while adjusting the channel dimension:

$$y^{encode} = Encoder_{pan}(pan\downarrow), \quad (13)$$

where  $y^{encode} \in \mathbb{R}^{H \times W \times C}$  denotes the encoded feature map, whose channel dimension is aligned with that of the multi-frame MS images  $\{lrms_i\}_{i=1}^k$ .

Let  $y^{encode}(h, w) \in \mathbb{R}^C$  denote the feature vector at spatial location  $(h, w)$ . A  $1 \times 1$  conv is first applied to project the feature into the same embedding dimension as the multi-frame features. Next, layer normalization (LN) is applied, followed by a shared multi-layer perceptron (MLP) to perform position-wise mapping and generate *pan-guided* fusion embeddings:

$$\begin{aligned} y^{proj}(h, w) &= \text{Conv}_{1 \times 1}(y^{encode}(h, w)), \\ y_0(h, w) &= \text{MLP}(\text{LN}(y^{proj}(h, w))), \end{aligned} \quad (14)$$

where  $y^{proj}(h, w) \in \mathbb{R}^{C_{encode}}$ , and  $y_0(h, w) \in \mathbb{R}^{C_{encode}}$  serves as the *pan-guided* fusion token at spatial location

$(h, w)$ . Unlike a global learnable token, this fusion token is adaptively generated from local *pan* structural information, enabling it to reflect spatially varying geometric characteristics.

During fusion,  $MFIF_{fusion}$  follows the standard transformer encoder architecture to preserve adaptability to arbitrary numbers of input frames. Let  $x_i^{encode}(h, w) \in \mathbb{R}^{C_{encode}}$  denote the feature vector of the  $i$ -th frame at spatial location  $(h, w)$ . For each  $(h, w)$ , the multi-frame features  $\{x_i^{encode}(h, w)\}_{i=1}^k$  are combined with the corresponding *pan*-guided token  $y_0(h, w)$  to form an input sequence. This sequence is then processed by  $MFIF_{fusion}$ , which consists of  $M$  stacked transformer encoder blocks, each including multi-head self-attention (MSA), feed-forward networks (FFN), LN, and residual connections. After fusion, the output vector corresponding to  $y_0(h, w)$  token position is selected as the fused multi-frame representation at location  $(h, w)$ :

$$\begin{aligned} Seq_{in}(h, w) &= [y_0(h, w), \{x_i^{encode}(h, w)\}_{i=1}^k], \\ Seq_{out}(h, w) &= MFIF_{fusion}(Seq_{input}(h, w)), \\ MFIF_{fusion}(\cdot) &= \mathcal{T}^{(M)} \circ \mathcal{T}^{(M-1)} \circ \dots \circ \mathcal{T}^{(1)}(\cdot), \\ z(h, w) &= Seq_{out}(h, w)|_{index=0}, \end{aligned} \quad (15)$$

Here,  $Seq_{in}(h, w)$  denotes the input sequence,  $Seq_{out}(h, w)$  denotes the output sequence, and  $\mathcal{T}^{(m)}(\cdot)$  denotes the  $m$ -th transformer encoder block. The output vector corresponding to the  $y_0(h, w)$  position, denoted as  $z(h, w) \in \mathbb{R}^{C_{fusion}}$ , represents the fused feature at spatial location  $(h, w)$  obtained by aggregating multi-frame features.

By performing this fusion process in parallel over all spatial locations, the fused feature map is obtained as

$$x^{fusion} = \{z(h, w)\}_{h=1, w=1}^{H, W} \quad (16)$$

where  $x^{fusion} \in \mathbb{R}^{H \times W \times C_{fusion}}$  is the output of  $MFIF_{fusion}$  and is subsequently fed into  $MFIF_{decode}$ , MSIF module, and Fusion Composition module for further processing.

### 3.4 Loss Function

We adopt a supervised learning paradigm to train both *SatFusion* and *SatFusion\** in an end-to-end manner. Since RS image fusion simultaneously involves *spatial structure reconstruction* and *spectral consistency preservation*, we design a weighted combination of multiple loss functions to jointly optimize texture details and spectral characteristics.

$$\begin{aligned} \mathcal{L}_{\text{total}} &= \lambda_1 \cdot \mathcal{L}_{\text{MAE}}(SR, GT) + \lambda_2 \cdot \mathcal{L}_{\text{MSE}}(SR, GT) \\ &\quad + \lambda_3 \cdot \mathcal{L}_{\text{SSIM}}(SR, GT) + \lambda_4 \cdot \mathcal{L}_{\text{SAM}}(SR, GT), \end{aligned} \quad (17)$$

Here  $\lambda_1, \lambda_2, \lambda_3$ , and  $\lambda_4$  are the corresponding weights, satisfying  $\lambda_1 + \lambda_2 + \lambda_3 + \lambda_4 = 1$ ,  $SR \in \mathbb{R}^{\gamma H \times \gamma W \times C}$  denotes the reconstructed high-resolution MS image produced by network, and  $GT \in \mathbb{R}^{\gamma H \times \gamma W \times C}$  represents the corresponding GT image.  $\mathcal{L}_{MAE}$  and  $\mathcal{L}_{MSE}$  are employed to constrain pixel-wise reconstruction errors and are widely adopted as supervision signals in both MFSR and Pansharpening networks. Building upon these pixel-level constraints, we further introduce structural and spectral supervision.

Specifically,  $\mathcal{L}_{SSIM}$  measures the similarity between  $SR$  and  $GT$  in terms of local structures and textures [47], which helps improve the fidelity of spatial details.  $\mathcal{L}_{SAM}$  enforces spectral consistency by constraining the spectral angle between  $SR$  and  $GT$  [24], effectively mitigating spectral distortions introduced during multi-source fusion. By jointly incorporating these loss, the proposed framework achieves collaborative optimization over two critical dimensions, *i.e.*, spatial structural accuracy and spectral consistency, which is particularly important for multi-frame and multi-source RS image fusion tasks.

#### 4 Datasets, Training and Evaluation

In this section, we introduce the datasets used in our experiments, the training settings, and the evaluation objectives.

##### 4.1 Datasets

The WorldStrat dataset [4] provides, for each geographic location, high-resolution image acquired from a single visit of SPOT 6/7 and multiple low-resolution MS images acquired from repeated visits of Sentinel-2. The high-resolution data include both a PAN image and an MS image. Notably, as a real satellite dataset, WorldStrat does not exclude low-quality frames from the multi-frame observations, making it more representative of real-world conditions. As discussed in Sec. 2.1, evaluating MFSR requires paired samples of the form  $\langle \{lr_i\}_{i=1}^k, GT \rangle$ . Since WorldStrat contains multi-frame low-resolution images together with high-resolution GT, it has been widely adopted for MFSR evaluation.

The WV3, QB, and GF2 datasets [6] provide, for each scene, one high-resolution PAN image and one low-resolution MS image, and are therefore commonly used for evaluating Pansharpening. As described in Sec. 2.2, Pansharpening evaluation requires datasets with paired samples of the form  $\langle lrms, pan, GT \rangle$ . Since the original datasets do not directly satisfy this requirement, most existing works construct simulated datasets using the Wald protocol [43], as illustrated in Fig. 5(a).

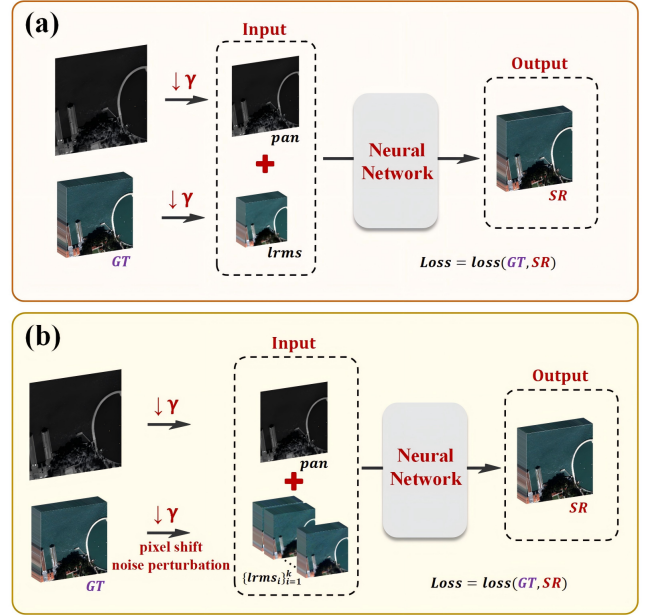


Fig. 5: (a) Workflow for constructing simulated datasets using Wald protocol. (b) Workflow for constructing simulated datasets with additional perturbations based on Alg. 1.

We conduct experiments on both real-world and simulated datasets. For the real-world WorldStrat dataset, *SatFusion* and *SatFusion\** are trained and evaluated directly using the provided multi-frame low-resolution MS images, high-resolution MS image, and high-resolution PAN image. For the WV3, QB, and GF2 datasets, we construct simulated data following the procedure illustrated in Fig. 5(b). Unlike the Wald protocol widely adopted in the Pansharpening literature, which enforces strict spatial alignment between *lrms* and *pan* and does not account for common misalignment and noise in real scenarios [43], we adopt a physics-inspired image formation strategy to generate more realistic observations.

As summarized in Alg. 1, we first apply random sub-pixel translations to the original MS images to simulate spatial misalignment caused by satellite attitude variations and orbital shifts. Next, Gaussian blurring with varying scales is introduced to approximate the sensor point spread function (PSF) and modulation transfer function (MTF) effects. The blurred images are then downsampled to obtain low-resolution observations. Finally, Poisson noise and Gaussian readout noise are added to the downsampled images to model the combined effects of photon noise and sensor noise in real imaging processes. Through this simulation pipeline, we generate, for each scene, a set of  $\{lrms_i\}_{i=1}^k$  with spatial misalignment and noise perturbations. Moreover,

**Algorithm 1** Physics-Inspired  $\{lrms_i\}_{i=1}^k$  Synthesis

**Require:** High-resolution MS image  $hrms \in \mathbb{R}^{\gamma H \times \gamma W \times C}$ ; PSF blur range  $\sigma \in [\sigma_{\min}, \sigma_{\max}]$ ; sub-pixel shift range  $\Delta \in [\Delta_{\min}, \Delta_{\max}]$ ; shot noise gain  $g$ ; readout noise standard deviation  $\sigma_r$

**Ensure:** Multi-frame low-resolution MS set  $\{lrms_i\}_{i=1}^k$

```

1: for  $i = 1$  to  $k$  do
2:   Sample sub-pixel shifts  $(\delta_x, \delta_y) \sim \mathcal{U}(\Delta)$ 
3:    $hrms_i \leftarrow \text{Warp}(hrms, \delta_x, \delta_y)$   $\triangleright$  Sub-pixel spatial misalignment
4:   Sample blur scale  $\sigma \sim \mathcal{U}([\sigma_{\min}, \sigma_{\max}])$ 
5:    $\widetilde{hrms}_i \leftarrow \text{GaussianBlur}(hrms_i, \sigma)$   $\triangleright$  Sensor PSF / MTF simulation
6:    $lrms_i \leftarrow \text{Downsample}(\widetilde{hrms}_i, \gamma)$   $\triangleright$  Spatial resolution degradation
7:   if  $g > 0$  then
8:      $lrms_i \leftarrow lrms_i + \mathcal{N}(0, \sqrt{lrms_i/g})$   $\triangleright$  Shot noise (Gaussian approximation)
9:   end if
10:   $lrms_i \leftarrow lrms_i + \mathcal{N}(0, \sigma_r^2)$   $\triangleright$  Readout noise
11: end for
12: return  $\{lrms_i\}_{i=1}^k$ 
```

the introduced sub-pixel shifts and degradations also lead to imperfect alignment between the low-resolution MS observations and the corresponding PAN image, further reflecting real-world scenarios. As a result, the constructed dataset is more challenging and better approximates practical satellite imaging conditions.

## 4.2 Training

We compare *SatFusion* and *SatFusion\** with a set of representative classical and recent MFSR and Pansharpening methods as baselines. To ensure a fair comparison, all methods are trained under identical experimental settings, including training configurations (e.g., number of epochs, batch size, and optimizer) and data-related parameters (e.g.,  $H$ ,  $W$ ,  $C$ ,  $\gamma$ , and  $k$ ). All experiments are conducted on a server equipped with eight NVIDIA RTX 4090 GPUs, and the experimental code has been made publicly available.

Prior MFSR studies have pointed out that, due to differences in acquisition conditions between multi-frame low-resolution inputs and high-resolution target images, the reconstructed *SR* and the *GT* may exhibit horizontal or vertical shifts as well as global brightness discrepancies [2, 3, 7, 8, 33, 38]. When training and testing on real-world datasets, directly comparing *SR* and *GT* without compensation may introduce additional interference. Following the protocol adopted for the WorldStrat dataset, we apply spatial shift correction and global brightness alignment [4] to the reconstructed *SR* prior to loss computation during training and prior to quantitative evaluation during testing for all experiments on

WorldStrat. This step is consistently applied across all methods, ensuring a fair and unbiased comparison.

## 4.3 Evaluation

We conduct extensive experiments to answer the following research questions:

**RQ1:** How do *SatFusion* and *SatFusion\** perform compared to baseline methods on real-world datasets?

**RQ2:** How do *SatFusion* and *SatFusion\** perform compared to baseline methods on simulated datasets?

**RQ3:** How do the number of input frames  $k$  and the super-resolution scale factor  $\gamma$  affect model performance?

**RQ4:** How well do the models generalize under different levels of noise perturbations and when the number of input frames differs between training and inference?

**RQ5:** How do the designs of individual modules and the choice of loss functions influence the performance of *SatFusion* and *SatFusion\**?

We evaluate all methods using a comprehensive set of quantitative metrics, including PSNR, SSIM, SAM [58], ERGAS [1], MAE, and MSE. In addition, qualitative evaluations are provided through visual comparisons of reconstructed images and corresponding error maps. Detailed experimental results and analyses are presented in Sec. 5.

## 5 Experiments

In this section, we present the experimental results along with corresponding analyses. The results on four datasets are reported in Sec. 5.1 and 5.2, addressing **RQ1** and **RQ2**. In Sec. 5.3, we investigate the impact of key hyperparameters to answer **RQ3**. In Sec. 5.4, we evaluate the generalization performance by varying the input images, addressing **RQ4**. Finally, Sec. 5.5 provides ablation studies to analyze the contribution of individual modules and loss functions, answering **RQ5**.

### 5.1 Results on WorldStrat

We conduct experiments on the original WorldStrat real-world dataset and additionally construct simulated data on WorldStrat using Alg. 1 to evaluate the performance of *SatFusion*, *SatFusion\**, and baseline methods. For *SatFusion* and *SatFusion\**, the inputs consist of  $\{lrms_i\}_{i=1}^{k=8}$  together with the corresponding *pan*. For MFSR methods, only  $\{lrms_i\}_{i=1}^{k=8}$  are used as inputs, while for Pansharpening methods, one *lrms* is randomly selected from  $\{lrms_i\}_{i=1}^{k=8}$  and fused with *pan*.

WorldStrat dataset provides official MFSR baseline implementations, including Multi-Frame SRCNN (denoted as MF-SRCNN [4]) and HighRes-Net [7]. In addition, we include other representative MFSR methods (RAMS [38] and TR-MISR [2]) and Pansharpening methods (PNN [30], PanNet [54], U2Net [35], Pan-Mamba [15], and ARConv [45]) as baselines. All methods are trained under identical experimental settings to ensure fair comparison, including the same loss function (Eq. 17) and the same optimizer (the Adam optimizer with a Cosine Annealing Warm Restart scheduler [29]). The spatial upscaling factor is set to  $\gamma = 3$ , and the loss weights are fixed to  $\lambda_1 = 0.3$ ,  $\lambda_2 = 0.3$ ,  $\lambda_3 = 0.2$ , and  $\lambda_4 = 0.2$ .

Table 1 reports the quantitative results of evaluated methods. Owing to the unified fusion interfaces of *SatFusion*, namely *MFIF*<sub>fusion</sub> and *MSIF*<sub>fusion</sub>, multi-frame fusion modules from MFSR and multi-source fusion modules from Pansharpening can be seamlessly integrated into the *SatFusion* (Sec. 3.2), resulting in multiple *SatFusion* variants. For *SatFusion*<sup>\*</sup>, the *MFIF* module is specifically redesigned as described in Sec. 3.3, while the *MSIF* module remains flexible to incorporate existing Pansharpening fusion components.

As shown in Table 1, *SatFusion* consistently outperforms the baseline methods. Compared to MFSR, *SatFusion* achieves an average improvement of **25.1%** in PSNR and an average reduction of **69.6%** in ERGAS. Compared to Pansharpening, it yields an average PSNR gain of **2.2%** and an ERGAS reduction of **12.0%**. Furthermore, *SatFusion*<sup>\*</sup> delivers additional performance gains over *SatFusion*, indicating that jointly modeling multi-frame and multi-source observations within a unified feature space significantly enhances feature fusion capability. Qualitative comparisons are visualized in Fig. 6. It can be clearly observed that *SatFusion* and *SatFusion*<sup>\*</sup>, which incorporate fine-grained structural details from *pan*, produce substantially higher-quality reconstructions than MFSR that rely solely on multi-frame information.

## 5.2 Results on WV3, QB, and GF2

We further evaluate *SatFusion* and *SatFusion*<sup>\*</sup> on the WV3, QB, and GF2 datasets using simulated data generated by Alg. 1, in order to examine their advantages over Pansharpening. These datasets have been extensively studied in the Pansharpening literature, and the DLPan-Toolbox [6] provides official implementations of representative Pansharpening networks for all three datasets. Accordingly, we select six representative methods, including PNN [30], DiCNN [14], MSDCNN [57],

DRPNN [49], FusionNet [5], and U2Net [35], as baselines. When constructing *SatFusion*, we integrate the multi-frame fusion components from MFSR into the unified fusion interface *MFIF*<sub>fusion</sub>. For training, all baselines follow the configurations provided in the original codebase, including image settings, number of epochs, optimizers, and loss functions. To ensure a fair comparison, *SatFusion* and *SatFusion*<sup>\*</sup> adopt exactly the same training configurations as their corresponding baseline methods, with only the network architecture and loss formulation being modified.

As reported in Table 2, *SatFusion* consistently outperforms the Pansharpening baselines, achieving an average PSNR improvement of **2.7%** and an average ERGAS reduction of **9.6%**. Furthermore, *SatFusion*<sup>\*</sup> yields additional gains over *SatFusion*, demonstrating the effectiveness of incorporating multi-frame information to enhance image fusion quality. Fig. 7 visualizes the fused images as well as the corresponding error maps with respect to the GT, where *SatFusion*<sup>\*</sup> achieves the best visual performance.

## 5.3 Hyperparameter Study

To answer **RQ3**, we investigate the impact of the number of input multi-frame images  $k$  and the super-resolution scale factor  $\gamma$  in both *SatFusion* and *SatFusion*<sup>\*</sup>.

The design of the unified fusion interfaces, namely *MFIF*<sub>fusion</sub> and *MSIF*<sub>fusion</sub>, enables *SatFusion* and *SatFusion*<sup>\*</sup> to flexibly integrate fusion components from existing methods, resulting in multiple network instantiations. To ensure a fair and comprehensive comparison for answering the research questions raised in Sec. 4.3, while keeping the presentation concise, we fix representative backbone methods in the following experiments unless otherwise specified.

Specifically, on the real WorldStrat dataset, we adopt HighRes-Net as the representative MFSR method and PanNet as the representative Pansharpening method. The multi-frame fusion module of HighRes-Net and the multi-source fusion module of PanNet are used as the *MFIF*<sub>fusion</sub> and *MSIF*<sub>fusion</sub> components of *SatFusion*, respectively, while the multi-source fusion module of PNN is employed as the *MSIF*<sub>fusion</sub> component in *SatFusion*<sup>\*</sup>. On the simulated QB dataset, we select FusionNet as the representative Pansharpening method. The multi-frame fusion module from TR-MISR and the multi-source fusion module from FusionNet are adopted as the *MFIF*<sub>fusion</sub> and *MSIF*<sub>fusion</sub> components of *SatFusion*, respectively, while the multi-source fusion module of FusionNet is used as the *MSIF*<sub>fusion</sub> component in *SatFusion*<sup>\*</sup>.

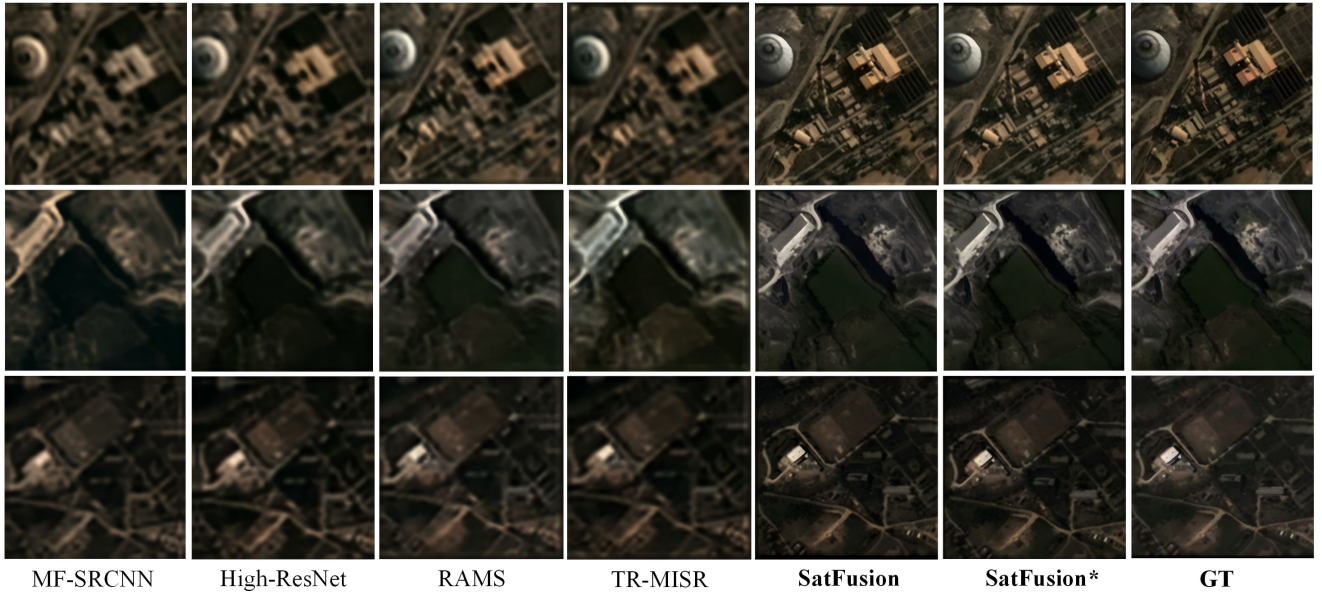


Fig. 6: Qualitative comparison of different fusion methods. *SatFusion* and *SatFusion\** produce visually superior reconstructions with sharper structures and clearer textures by effectively integrating fine-grained spatial details from the PAN image, compared to MFSR methods that rely solely on multi-frame information.

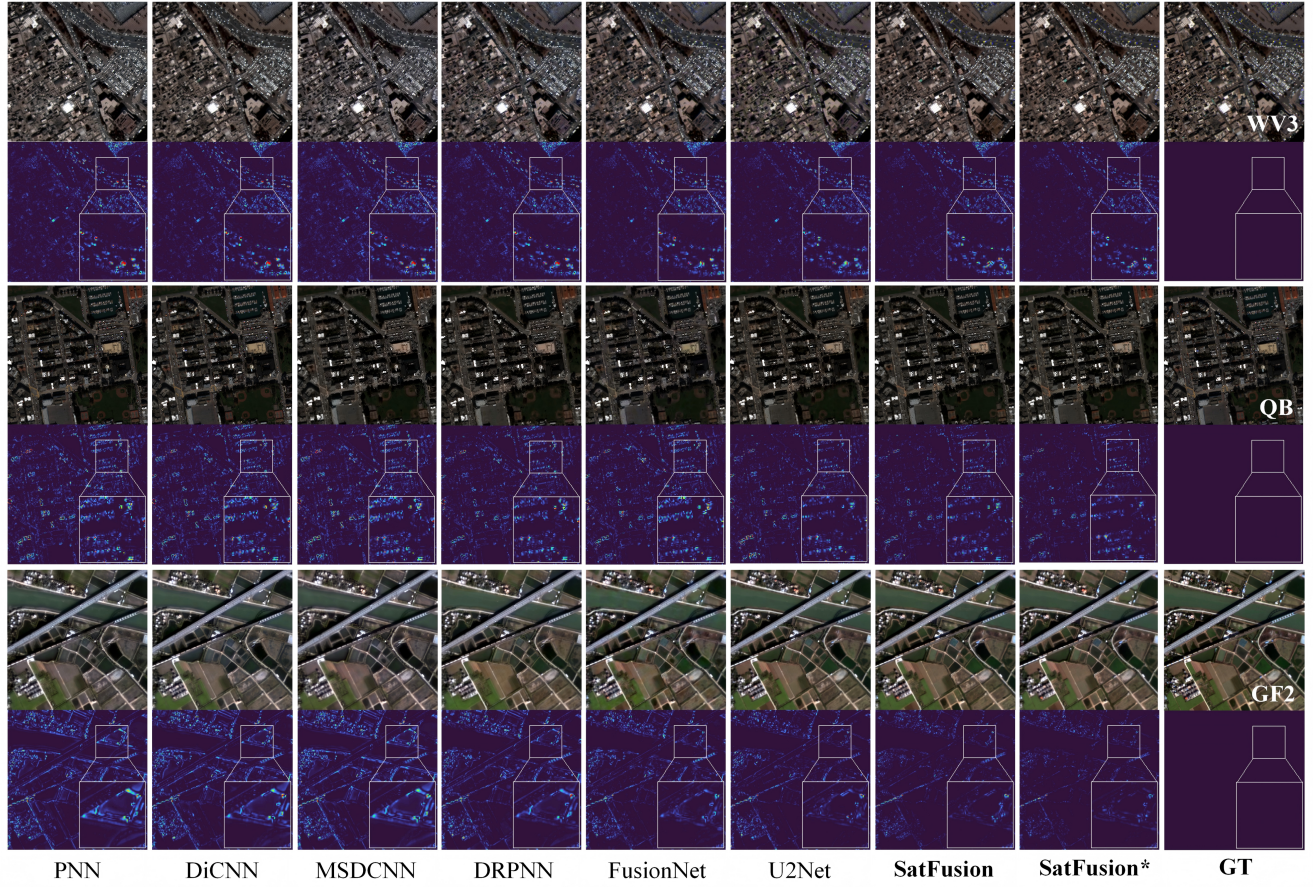


Fig. 7: Qualitative comparison of different fusion methods. The figure shows the fused images together with the corresponding error maps with respect to GT. Benefiting from the incorporation of multi-frame information, *SatFusion\** produces reconstructions with lower errors and superior visual quality compared to the baseline methods.

Table 1: Metrics on the WorldStrat Real (a) and Simulated (b) datasets.

Methods	(a) Metrics on the WorldStrat Real Dataset						(b) Metrics on the WorldStrat Synthetic Dataset						#Params	
	PSNR↑	SSIM↑	SAM↓	ERGAS↓	MAE↓	MSE↓	PSNR↑	SSIM↑	SAM↓	ERGAS↓	MAE↓	MSE↓		
MFSR	MF-SRCNN	36.8263	0.8767	2.6776	9.3946	1.4681	9.6654	39.0772	0.8964	2.4051	5.5574	1.0371	4.0053	1778.77K
	HighRes-Net	37.0815	0.8763	2.2503	9.1406	1.4498	9.5003	39.7523	0.9025	1.6448	5.1644	0.9519	3.4906	1627.98K
	RAMS	37.1946	0.8793	2.3063	8.8203	1.4097	9.1261	40.3275	0.9101	1.4961	4.7717	0.8771	3.0101	338.06K
	TR-MISR	37.0014	0.8778	2.3378	9.2222	1.4283	9.2299	39.3560	0.9005	1.7136	5.2308	0.9714	3.6965	470.35K
PanSharpen	<b>average</b>	37.0260	0.8775	2.3930	9.1444	1.4390	9.3804	39.6783	0.9024	1.8149	5.1811	0.9594	3.5506	
	PNN	46.4287	0.9877	2.1886	2.6345	0.4341	0.5246	47.5420	0.9886	1.9289	2.3656	0.4192	0.4289	76.04K
	PanNet	45.6398	0.9843	2.3978	3.0284	0.4836	0.6414	48.0819	0.9900	1.8248	1.9513	0.3376	0.3108	308.68K
	U2Net	46.8601	0.9859	2.2141	2.6720	0.4182	0.4750	47.4352	0.9910	1.9393	2.1106	0.3707	0.3519	632.81K
	Pan-Mamba	45.7723	0.9861	2.4807	2.8916	0.4606	0.5840	47.9158	0.9882	1.7338	2.0379	0.3451	0.3324	479.48K
	ARConv	46.6602	0.9864	2.2151	2.7638	0.4275	0.4944	46.8972	0.9873	2.0434	2.2976	0.3976	0.3897	15922.42K
	<b>average</b>	46.2722	0.9861	2.2993	2.7981	0.4448	0.5439	47.5744	0.9890	1.8940	2.1526	0.3740	0.3627	
	<i>MFIF<sub>fusion</sub></i>	<i>MSIF<sub>fusion</sub></i>												
MF-SRCNN	PNN	46.9912	0.9903	1.9501	2.4087	0.4037	0.4621	48.9561	0.9945	1.7296	1.8634	0.3113	0.2782	1853.20K
	PanNet	46.7910	0.9896	2.1471	2.5141	0.4100	0.4779	47.5788	0.9911	2.0159	2.2044	0.3735	0.3838	2085.84K
	U2Net	47.0066	0.9888	2.1659	2.5733	0.4130	0.4813	47.7126	0.9898	1.9826	2.1318	0.3710	0.3820	2409.97K
	Pan-Mamba	46.5703	0.9912	2.4536	2.4990	0.4190	0.5087	47.5974	0.9930	2.2166	2.1428	0.3647	0.3969	2256.63K
	ARConv	47.1350	0.9878	1.9386	2.5414	0.4059	0.4595	47.6784	0.9895	1.7688	2.1659	0.3764	0.3811	17699.58K
HighRes-Net	PNN	46.9310	0.9887	2.0203	2.5345	0.4041	0.4840	49.5682	0.9922	1.6734	1.6948	0.2925	0.2494	1702.42K
	PanNet	47.0376	0.9890	2.0267	2.4888	0.3978	0.4517	49.7340	0.9947	1.6652	1.6614	0.2855	0.2419	1935.06K
	U2Net	47.3020	0.9895	1.8844	2.4569	0.3981	0.4469	49.1785	0.9932	1.6735	1.7584	0.3130	0.2799	2259.18K
	Pan-Mamba	46.5283	0.9906	2.3986	2.5027	0.4196	0.5064	48.5836	0.9952	1.9645	1.9224	0.3262	0.2973	2105.85K
	ARConv	47.1686	0.9890	1.9508	2.7859	0.4038	0.4567	48.2011	0.9903	1.7761	1.9991	0.3553	0.3469	17548.80K
RAMS	PNN	47.1100	0.9907	1.9679	2.3450	0.3971	0.4610	50.0541	0.9928	1.4765	1.5354	0.2708	0.2126	412.49K
	PanNet	47.0404	0.9888	1.9705	2.4689	0.3993	0.4493	50.2041	0.9968	1.5331	1.5722	0.2647	0.2011	645.13K
	U2Net	47.5786	0.9913	1.8592	2.4918	0.3842	0.4174	48.6907	0.9902	1.7652	1.8493	0.3121	0.2754	969.26K
	Pan-Mamba	47.0081	0.9924	2.1994	2.5279	0.3987	0.4556	49.7599	0.9916	1.6422	1.6407	0.2783	0.2333	815.92K
	ARConv	47.1412	0.9877	1.9462	2.6387	0.4076	0.4584	48.7653	0.9892	1.6328	1.8581	0.3229	0.2757	16258.87K
TR-MISR	PNN	46.7560	0.9896	2.1167	2.5260	0.4174	0.4983	49.5353	0.9929	1.6156	1.6512	0.2914	0.2439	544.78K
	PanNet	46.9719	0.9898	1.9917	2.5176	0.4031	0.4688	49.6781	0.9928	1.6158	1.6158	0.2875	0.2510	777.42K
	U2Net	47.6068	0.9890	1.9046	2.4587	0.3814	0.4150	48.4520	0.9903	1.9849	1.9062	0.3373	0.3309	1101.55K
	Pan-Mamba	46.7936	0.9884	2.0236	2.4335	0.4112	0.4923	49.5882	0.9965	1.7126	1.6903	0.2892	0.2577	948.22K
	ARConv	47.4052	0.9889	1.9852	2.5244	0.3914	0.4334	48.2372	0.9913	1.7387	1.9963	0.3505	0.3320	16391.17K
<i>SatFusion*</i>	<b>average</b>	<b>47.0437</b>	<b>0.9896</b>	<b>2.0451</b>	<b>2.5119</b>	<b>0.4033</b>	<b>0.4642</b>	<b>48.8876</b>	<b>0.9924</b>	<b>1.7594</b>	<b>1.8430</b>	<b>0.3187</b>	<b>0.2926</b>	
	<i>MSIF<sub>fusion</sub></i>													
	PNN	47.2238	0.9898	1.9151	2.3275	0.3960	0.4472	49.8449	0.9935	1.6380	1.6256	0.2823	0.2414	545.48K
	PanNet	47.3154	0.9875	1.9136	2.3372	0.3881	0.4359	48.9527	0.9926	1.7839	1.7906	0.3139	0.2933	778.12K
	U2Net	47.7973	0.9878	1.8035	2.2640	0.3789	0.4147	49.4695	0.9911	1.6273	1.6910	0.2991	0.2626	1102.24K
<i>SatFusion*</i>	Pan-Mamba	47.0228	0.9872	2.0780	2.3900	0.3986	0.4586	49.7388	0.9960	1.7369	1.6620	0.2829	0.2408	948.91K
	ARConv	47.5509	0.9879	1.8447	2.3398	0.3840	0.4159	48.7734	0.9908	1.7211	1.8228	0.3289	0.3062	16391.85K
	<b>average</b>	<b>47.3820</b>	<b>0.9880</b>	<b>1.9110</b>	<b>2.3317</b>	<b>0.3891</b>	<b>0.4345</b>	<b>49.3559</b>	<b>0.9928</b>	<b>1.7014</b>	<b>1.7184</b>	<b>0.3014</b>	<b>0.2689</b>	

**Bold:** Best; Underline: Second best.

### 5.3.1 Effect of Input Image Number

We evaluate the effect of the number of input multi-frame images  $k$  on reconstruction quality on both the real WorldStrat dataset and the simulated QB dataset by varying  $k$  during training. As shown in Fig. 8, the image fusion performance generally improves as  $k$  increases, indicating that incorporating a larger number of multi-frame observations is beneficial for the model. This trend suggests that the network effectively exploits complementary information across multiple frames to enhance reconstruction quality. However, we observe that the performance gains gradually saturate when  $k$  becomes large. This phenomenon implies that while additional frames introduce more complementary information, they also bring increased noise and redundant content, which limits further performance improvement. Such saturation behavior is particularly evident on the real WorldStrat dataset, where low-quality frames are not filtered out.

### 5.3.2 Effect of Upscaling Factor

We investigate the impact of the super-resolution upscaling factor  $\gamma$  on reconstruction performance on the real

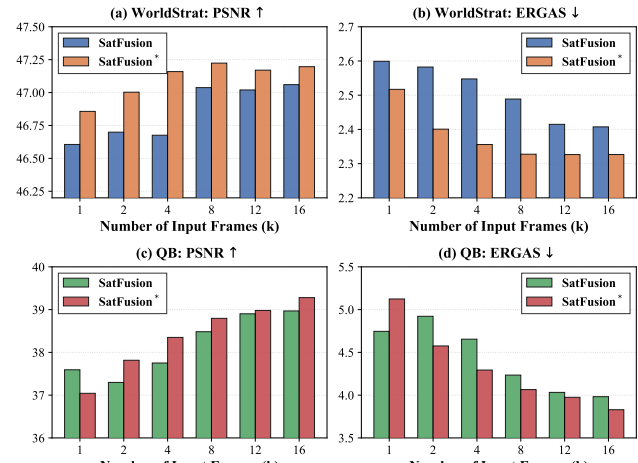


Fig. 8: Experimental results of the number of input frames  $k$  on (a, b) the WorldStrat dataset and (c, d) the QB dataset. We compare the PSNR and ERGAS metrics for both *SatFusion* and *SatFusion\**. The WorldStrat dataset. In addition to the results reported in Sec. 5.1 with  $\gamma = 3$ , we further conduct experiments with  $\gamma = 2$  and  $\gamma = 5$ , the internal upscaling parameter  $\gamma' = 2$  is kept fixed across all experiments. As shown in

Table 2: Experimental metrics on WV3, GF2, and QB datasets

Methods	WV3				GF2				QB				
	PSNR↑	SSIM↑	SAM↓	ERGAS↓	PSNR↑	SSIM↑	SAM↓	ERGAS↓	PSNR↑	SSIM↑	SAM↓	ERGAS↓	
Pansharpen	PNN	36.5340	0.9548	4.2758	3.6505	41.9402	0.9696	1.5319	1.4494	36.0032	0.9264	5.1423	5.7539
	DiCNN	37.1690	0.9611	4.0397	3.4236	42.4487	0.9729	1.4386	1.3750	36.2339	0.9305	4.9892	5.6132
	MSDCNN	35.9721	0.9454	4.7528	3.9338	42.0847	0.9702	1.5241	1.4278	35.8757	0.9254	5.1286	5.8496
	DRPN	37.1089	0.9603	4.1000	3.4253	43.1093	0.9760	1.3330	1.2747	37.3074	0.9436	4.7667	4.9032
	FusionNet	37.5678	0.9634	3.8872	3.2372	42.7230	0.9740	1.3562	1.3319	36.8057	0.9379	4.9236	5.1991
	U2Net	38.0416	0.9678	3.6772	3.0081	43.1198	0.9763	1.2491	1.2930	37.7626	0.9479	4.6238	4.6672
average		37.0656	0.9588	4.1221	3.4464	42.5710	0.9732	1.4055	1.3586	36.6648	0.9353	4.9290	5.3310
<i>MSIFusion</i> <i>MFIFusion</i>													
PNN	MF-SRCNN	36.8196	0.9608	4.3168	3.5191	41.8845	0.9724	1.6167	1.4753	36.0371	0.9279	5.1139	5.7658
	HighRes-Net	37.0614	0.9617	4.1264	3.4345	42.3180	0.9731	1.5600	1.4153	36.0488	0.9282	5.1232	5.7598
	RÄMS	37.1502	0.9607	4.0999	3.4178	42.7533	0.9736	1.4507	1.3559	36.5932	0.9331	4.9491	5.3915
	TR-MISR	36.8628	0.9619	4.1233	3.4616	42.6706	0.9736	1.4440	1.3639	36.1081	0.9300	5.0542	5.7149
DiCNN	MF-SRCNN	37.8822	0.9682	3.6145	3.1235	42.7883	0.9761	1.2998	1.3574	37.5458	0.9486	4.4724	4.7414
	HighRes-Net	38.6588	0.9714	3.3471	2.8626	43.4098	0.9772	1.1542	1.2752	37.8274	0.9504	4.3736	4.6255
	RÄMS	38.4515	0.9716	3.3458	2.9224	43.2552	0.9764	1.1565	1.2817	38.3380	0.9555	4.2156	4.2813
	TR-MISR	38.3025	0.9709	3.4684	2.9962	44.3630	0.9806	1.0832	1.1274	37.5241	0.9484	4.3801	4.7971
MSDCNN	MF-SRCNN	36.6887	0.9590	4.2955	3.5976	42.4895	0.9743	1.4321	1.3893	36.1084	0.9335	4.7937	5.6581
	HighRes-Net	36.7270	0.9594	4.3319	3.5825	43.0057	0.9760	1.3138	1.3177	35.9599	0.9324	4.8643	5.7786
	RÄMS	36.8621	0.9605	4.1827	3.5228	43.1134	0.9760	1.3203	1.3107	36.2425	0.9341	4.7583	5.5703
	TR-MISR	36.8286	0.9605	4.1982	3.5319	42.9072	0.9751	1.3560	1.3379	36.3045	0.9349	4.7946	5.3322
DRPN	MF-SRCNN	37.0290	0.9632	4.0149	3.4516	43.6850	0.9789	1.2164	1.2196	37.7417	0.9513	4.4960	4.6487
	HighRes-Net	37.4433	0.9654	3.7812	3.3273	44.3259	0.9807	1.1437	1.1412	38.1620	0.9551	4.3119	4.3766
	RÄMS	37.5732	0.9655	3.7671	3.2905	44.6619	0.9819	1.1479	1.0826	38.2824	0.9552	4.2797	4.3140
	TR-MISR	37.4104	0.9650	3.8038	3.3520	45.0867	0.9829	1.0532	1.0317	38.2458	0.9559	4.2735	4.3351
FusionNet	MF-SRCNN	37.8537	0.9688	3.7209	3.1390	43.3958	0.9776	1.1749	1.2756	37.9621	0.9538	4.3859	4.4830
	HighRes-Net	38.5889	0.9728	3.3880	2.8749	43.7922	0.9782	1.1204	1.2290	38.3800	0.9569	4.1744	4.2750
	RÄMS	38.3149	0.9708	3.3861	2.9825	43.6333	0.9766	1.1063	1.2347	38.4529	0.9574	4.1426	4.2295
	TR-MISR	38.6914	0.9729	3.3040	2.8482	44.5058	0.9816	1.1027	1.1054	38.4834	0.9581	4.1139	4.2345
U2Net	MF-SRCNN	38.1168	0.9698	3.5777	2.9076	43.1605	0.9783	1.2364	1.2449	37.8251	0.949	4.6643	4.7903
	HighRes-Net	37.3474	0.9641	4.0147	3.3194	43.7863	0.9793	1.1252	1.2076	37.9579	0.9517	4.5857	4.5578
	RÄMS	39.2459	0.9641	4.0147	3.3194	43.7863	0.9793	1.1252	1.2076	37.9579	0.9517	4.5857	4.5578
	TR-MISR	39.1302	0.9753	3.0939	2.6848	44.2919	0.9815	1.0925	1.1344	38.6255	0.9590	4.1474	4.1469
average		37.7100	0.9665	3.7672	3.2003	43.5206	0.9778	1.2373	1.2475	37.4679	0.9466	4.5274	4.8447
<i>MSIFusion</i>													
SatFusion*	PNN	37.3092	0.9627	4.0141	3.3731	42.8426	0.9744	1.4201	1.3407	36.2618	0.9307	5.0586	5.6360
	DiCNN	38.3609	0.9710	3.4074	2.9532	45.8234	0.9864	0.9959	0.9337	38.6826	0.9595	4.1140	4.1168
	MSDCNN	36.8714	0.9584	4.4364	3.5939	43.0315	0.9761	1.3360	1.3027	36.4599	0.9350	4.7822	5.5434
	DRPN	37.4506	0.9655	3.8028	3.3206	44.9421	0.9826	1.0710	1.0491	38.1898	0.9553	4.3033	4.3701
	FusionNet	39.0767	0.9748	3.1360	2.7155	45.5417	0.9862	1.0247	0.9738	38.7960	0.9605	4.0505	4.0650
	U2Net	39.1022	0.9762	3.1035	2.7015	45.3869	0.9847	0.9989	1.0013	38.2583	0.9572	4.3039	4.2850
average		<b>38.0285</b>	<b>0.9681</b>	<b>3.6500</b>	<b>3.1096</b>	<b>44.5947</b>	<b>0.9817</b>	<b>1.1411</b>	<b>1.1002</b>	<b>37.7747</b>	<b>0.9497</b>	<b>4.4346</b>	<b>4.6694</b>

**Bold:** Best; Underline: Second best.

Table 3, both *SatFusion* and *SatFusion\** consistently achieve the best performance under different upscaling factors. Notably, as  $\gamma$  increases, the reconstruction task becomes progressively more challenging, leading to a general degradation in performance metrics; nevertheless, even under the highly challenging setting of  $\gamma = 5$ , where fine-grained details are particularly difficult to recover, our method is able to maintain stable and relatively high reconstruction quality.

#### 5.4 Generalization Evaluation

On the simulated QB dataset, we evaluate the generalization ability of the model by testing its performance when facing input images with different noise levels at inference stage, as well as when the number of input images at inference differs from that used during training, thereby answering **RQ4**.

##### 5.4.1 Robustness to Image Quality Variations

By adjusting the parameter  $g$  in Alg. 1 (with smaller  $g$  indicating stronger noise perturbations), we vary the

Table 3: Quantitative results at different  $\gamma$ .

$\gamma$	Method	PSNR↑	SSIM↑	SAM↓	ERGAS↓
$\gamma = 2$	MFSR	37.4654	0.8832	2.3514	8.1199
	Pansharpening	46.1225	0.9801	2.7920	4.0084
	<u><i>SatFusion</i></u>	<u>47.9195</u>	<b>0.9912</b>	<u>1.8548</u>	<u>2.2721</u>
	<i>SatFusion*</i>	<b>48.0910</b>	<u>0.9898</u>	<b>1.7931</b>	<b>2.1879</b>
$\gamma = 3$	MFSR	37.0815	0.8763	2.2503	9.1406
	Pansharpening	45.6398	0.9843	2.3978	3.0284
	<u><i>SatFusion</i></u>	<u>47.0376</u>	<u>0.9890</u>	<u>2.0267</u>	<u>2.4888</u>
	<i>SatFusion*</i>	<b>47.2238</b>	<b>0.9898</b>	<b>1.9151</b>	<b>2.3275</b>
$\gamma = 5$	MFSR	35.9801	0.8605	2.4485	8.1229
	Pansharpening	44.8784	0.9805	2.7607	3.2184
	<u><i>SatFusion</i></u>	<u>45.9070</u>	<b>0.9870</b>	<b>2.1466</b>	2.5871
	<i>SatFusion*</i>	<b>46.2071</b>	<u>0.9855</u>	<u>2.1840</u>	<b>2.5509</b>

**Bold:** Best; Underline: Second best.

noise intensity during inference to emulate the instabilities commonly encountered in RS images. As shown in Fig. 9, both *SatFusion* and *SatFusion\** consistently outperform Pansharpening methods across different noise levels. This demonstrates that exploiting complementary information from multiple frames effectively mitigates noise interference, allowing the proposed framework to

retain robust and stable performance in challenging scenarios such as image blur.

#### 5.4.2 Generalization to Input Image Number

Unlike Sec. 5.3.1, we evaluate the model’s generalization by varying the number of input frames  $k$  during inference, i.e., when it differs from training. This aspect is often overlooked in many MFSR methods. For example, MF-SRCNN and RAMS concatenate multi-frame features along the channel dimension and perform fusion via conv, which requires the number of input frames during inference to match that during training. In contrast, HighRes-Net, which employs recursive conv fusion, and TR-MISR, which utilizes a transformer-based architecture, support arbitrary numbers of input frames at inference. Accordingly, in *SatFusion*, we adopt the multi-frame fusion modules from HighRes-Net and TR-MISR as the  $MFIF_{fusion}$  component.

Fig 10 illustrates the reconstruction quality as  $k$  varies, where all test points are inferred using models trained with  $k = 8$ . We observe three phenomena: First, transformer-based *SatFusion* and *SatFusion\** effectively adapt to variable-length input scenarios due to their self-attention mechanism. Second, as the number of input frames  $k$  increases, the fusion quality initially improves, benefiting from the additional complementary information. However, when  $k$  becomes too large, performance declines because (i) additional frames introduce more noise along with complementary information, and (ii) the discrepancy between training and inference frame counts grows, degrading fusion quality. Finally, *SatFusion\** consistently achieves the best reconstruction quality across all test points, demonstrating its superior generalization capability.

### 5.5 Ablation Study

To address **RQ5**, we conduct ablation studies on the WorldStrat real-world dataset and the QB simulated dataset, systematically evaluating the contributions of each module and loss component.

#### 5.5.1 Effect of Modules

We perform ablation studies on *SatFusion* and *SatFusion\** by removing the MFIF Module, MSIF Module, and Fusion Composition (FC) Module, to analyze the contribution of each module to overall reconstruction quality. It is worth noting that when the MFIF Module is ablated, *SatFusion* and *SatFusion\** randomly select one *lrms* image and the corresponding *pan* as input,

and the *lrms* is upsampled and aligned to the *pan* spatial dimensions in the same manner as Pansharpening, followed by processing through the MSIF Module and FC Module.

Table 4 shows the results. Ablating the MSIF Module causes the model to lose fine-grained texture features, while removing the MFIF Module results in the loss of complementary information from multiple frames, leading to significant drops in performance metrics. This demonstrates that collaboratively modeling multi-frame and multi-source features in the same feature space enhances feature fusion capabilities. Ablating the FC Module results in a moderate decline in metrics, indicating its role in adaptively leveraging the advantages of multi-frame and multi-source images.

Table 4: Quantitative ablation results of key components in *SatFusion*, including MSIF, MFIF, and FC modules.

Meth.	Data.	MFIF	MSIF	FC	PSNR $\uparrow$	SSIM $\uparrow$	SAM $\downarrow$	ERGAS $\downarrow$
<i>SatFusion</i>	WS	✗	✓	✓	45.9802	0.9847	2.2177	2.8256
		✓	✗	✓	37.0787	0.8758	2.2510	9.1041
		✓	✓	✗	46.3395	<b>0.9896</b>	2.2861	2.5255
		✓	✓	✓	<b>47.0376</b>	0.9890	<b>2.0267</b>	<b>2.4888</b>
<i>SatFusion*</i>	QB	✗	✓	✓	37.0025	0.9422	4.7216	5.0986
		✓	✗	✓	33.3935	0.8627	5.5241	7.8642
		✓	✓	✗	38.3977	0.9570	4.1362	4.2728
		✓	✓	✓	<b>38.4834</b>	<b>0.9581</b>	<b>4.1139</b>	<b>4.2345</b>
<i>SatFusion*</i>	WS	✗	✓	✓	46.3021	0.9852	2.1617	2.6767
		✓	✗	✓	40.2804	0.9330	1.9746	4.9765
		✓	✓	✗	46.9979	0.9873	1.9432	2.4328
		✓	✓	✓	<b>47.2238</b>	<b>0.9898</b>	<b>1.9151</b>	<b>2.3275</b>
<i>SatFusion*</i>	QB	✗	✓	✓	37.0025	0.9422	4.7216	5.0986
		✓	✗	✓	34.2252	0.8881	5.2789	7.0944
		✓	✓	✗	<b>38.8061</b>	0.9603	4.0557	4.0723
		✓	✓	✓	38.7960	<b>0.9605</b>	<b>4.0505</b>	<b>4.0650</b>

**Bold:** Best; WS: WorldStrat; ✓: w, ✗: w/o.

#### 5.5.2 Effect of *SatFusion\**

As introduced in Sec. 3.3, *SatFusion\** optimizes the MFIF Module compared to *SatFusion*, specifically in the  $MFIF_{encode}$  and  $MFIF_{fusion}$ . We conduct ablation studies by removing the reference *pan* in  $MFIF_{encode}$  (denoted as  $E_{pan}$ ) and the position-adaptive embedding vector generated from *pan* in  $MFIF_{fusion}$  (denoted as  $T_{pan}$ ), replacing them with global embedding vectors. As shown in Table 5, *SatFusion\** outperforms *SatFusion* in fusion quality. Ablating  $E_{pan}$  or  $T_{pan}$  leads to a drop in performance metrics, demonstrating that the spatially adaptive multi-frame feature aggregation in *SatFusion\** effectively enhances the coupling and fusion capability of multi-frame and multi-source features.

#### 5.5.3 Effect of Loss Functions

We design different weighted combinations of loss functions to supervise the reconstruction results, jointly

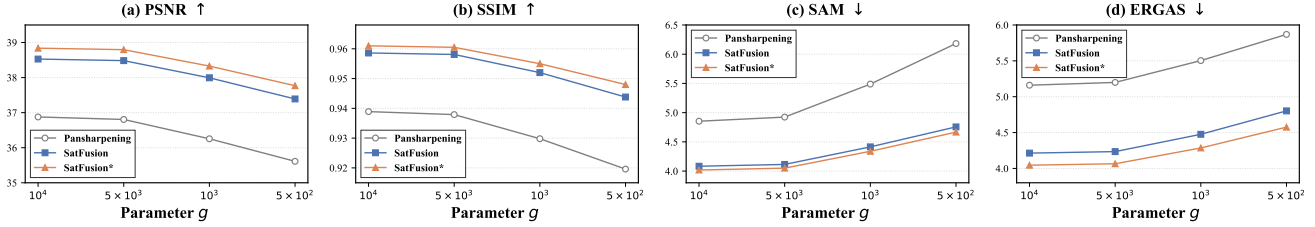


Fig. 9: Robustness analysis against noise perturbations by varying the parameter  $g$  (trained at  $g = 5 \times 10^3$ ). (a-d) represent PSNR ( $\uparrow$ ), SSIM ( $\uparrow$ ), SAM ( $\downarrow$ ), and ERGAS ( $\downarrow$ ) respectively. Across different noise levels, *SatFusion* and *SatFusion*\* consistently outperform Pansharpening methods.

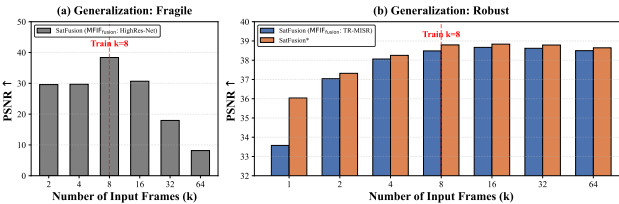


Fig. 10: Generalization analysis across varying inference frames  $k$  (trained at  $k = 8$ ). (a) exhibits fragile generalization, with performance collapsing as  $k$  deviates from the training setting. (b) Transformer-based variants demonstrate robust generalization, where *SatFusion*\* consistently maintains superior and stable PSNR even up to  $k = 64$ .

Table 5: Quantitative ablation results of *SatFusion*\*.

Data.	Method	$E_{pan}$	$T_{pan}$	PSNR↑	SSIM↑	SAM↓	ERGAS↓
WS	<i>SatFusion</i>	×	×	46.7559	0.9896	2.1167	2.5260
	<i>SatFusion</i>	×	✓	47.0941	0.9909	1.9774	2.3694
	<i>SatFusion</i> *	✓	×	47.1625	<b>0.9927</b>	1.9191	2.3324
	<i>SatFusion</i> *	✓	✓	<b>47.2238</b>	0.9898	<b>1.9151</b>	<b>2.3275</b>
QB	<i>SatFusion</i>	×	×	38.4834	0.9581	4.1139	4.2345
	<i>SatFusion</i>	×	✓	38.5267	0.9586	4.1207	4.1904
	<i>SatFusion</i> *	✓	×	38.6889	0.9597	4.0760	4.1343
	<i>SatFusion</i> *	✓	✓	<b>38.7960</b>	<b>0.9605</b>	<b>4.0505</b>	<b>4.0650</b>

**Bold:** Best; ✓: w, ×: w/o.

optimizing image texture and spectral features. We perform ablation studies on the composition of the loss functions. As shown in Table 6, the worst-performing metrics are highlighted in bold, while the second-worst metrics are underlined. Removing any loss component leads to a significant drop in certain metrics, confirming that multi-loss optimization plays a crucial role in balancing texture fidelity and spectral quality.

## 6 Discussion

In this section, we analyze the factors contributing to the performance improvements of our approach over exist-

Table 6: Quantitative results with different loss functions.

Meth.	Data.	$\mathcal{L}_{MAE}$	$\mathcal{L}_{MSE}$	$\mathcal{L}_{SSIM}$	$\mathcal{L}_{SAM}$	PSNR↑	SSIM↑	SAM↓	ERGAS↓
<i>SatFusion</i>	WS	✓	✓	✓	✓	47.0376	0.9898	2.0267	2.4888
	WS	✓	✓	✓	✗	47.2490	0.9903	<u>2.2524</u>	2.3342
	WS	✓	✓	✗	✓	46.0729	<u>0.9878</u>	2.1005	<u>2.7682</u>
	WS	✗	✓	✗	✗	<b>43.6225</b>	<b>0.9735</b>	<b>3.3837</b>	<b>3.4150</b>
<i>SatFusion</i>	QB	✓	✓	✓	✓	38.4834	0.9581	4.1139	4.2345
	QB	✓	✓	✓	✗	<b>38.4271</b>	0.9577	<b>4.1654</b>	4.2483
	QB	✓	✓	✗	✓	38.4463	<u>0.9573</u>	4.0887	4.265
	QB	✗	✓	✗	✗	<b>38.3706</b>	<b>0.9562</b>	<b>4.2233</b>	<b>4.2926</b>
<i>SatFusion</i> *	WS	✓	✓	✓	✓	47.2238	0.9898	1.9151	2.3275
	WS	✓	✓	✓	✗	47.4381	0.9901	<b>1.9416</b>	2.2670
	WS	✓	✓	✗	✓	<b>46.4639</b>	<u>0.9879</u>	1.8993	2.6645
	WS	✗	✓	✗	✗	<b>43.6317</b>	<b>0.9804</b>	<b>3.3028</b>	<b>3.3784</b>
<i>SatFusion</i> *	QB	✓	✓	✓	✗	38.7960	0.9605	4.0505	4.0650
	QB	✓	✓	✓	✗	<b>38.7492</b>	0.9603	<b>4.0702</b>	4.077
	QB	✓	✓	✗	✓	38.7926	0.9601	4.0058	<u>4.0892</u>
	QB	✗	✓	✗	✗	<b>38.6660</b>	<b>0.9586</b>	<b>4.1283</b>	<b>4.1380</b>

**Bold:** Worst; Underline: Second worst; ✓: w, ×: w/o.

ing MFSR and Pansharpening methods (Sec. 6.1), and discuss the practical implications of this work (Sec. 6.2).

### 6.1 Advantages over Pansharpening

The experimental results demonstrate that *SatFusion* and *SatFusion*\* outperform both MFSR and Pansharpening. The introduction of fine-grained texture features leads to a substantial improvement in the reconstructed image quality over MFSR, which is intuitive. Here, we focus on analyzing the reasons behind the performance gain over Pansharpening.

As discussed in Sec. 5.3.1 and Sec. 5.4.2, the model can leverage complementary information present in multiple frames to enhance performance. In addition, we conduct a “stress test” experiment on the QB simulated dataset. For the Pansharpening, we follow the original Wald protocol (Fig. 5(a)) to construct the dataset, without introducing image misalignment or noise. In contrast, *SatFusion*\* uses the dataset construction shown in Fig. 5(b), which includes both misalignment and noise. It is worth noting that the input image quality for *SatFusion*\* is significantly lower than that for Pansharpening. As shown in Fig. 11, as the number of input frames increases, *SatFusion*\* is able to leverage

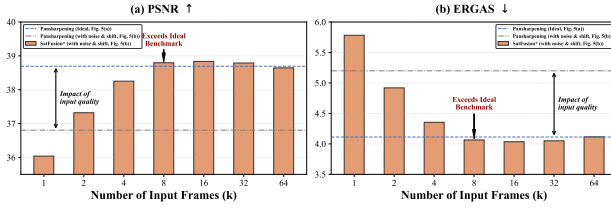


Fig. 11: Comparison between *SatFusion\** and Pansharpening. Horizontal lines represent Pansharpening under ideal (Fig. 5(a)) and adverse (Fig. 5(b)) conditions. Pansharpening is sensitive to input quality, *SatFusion\** leverages multi-frame fusion to mitigate degradation, eventually surpassing even the ideal-case single-frame benchmark as  $k$  increases.

the complementary information in multiple frames to surpass Pansharpening, even when the overall input image quality is poor.

## 6.2 Real-World Implications

**Enhancing image quality.** As an end-to-end unified framework, our approach can significantly enhance the quality of the fused images. Compared to MFSR that only leverage multi-frame data, our approach incorporates the spatial details from PAN image. Compared to Pansharpening, which align low-resolution images to high-resolution ones via single-image interpolation, our approach achieves alignment in the high-resolution feature space formed by fusing multiple complementary low-resolution frames, maintaining stable performance even in complex scenarios. This not only alleviates the conflict between low-quality redundant data and user demand for high-quality data but also better reflects practical application scenarios.

**Reducing image redundancy.** Traditional approaches typically store and transmit multiple images, leading to redundant transmission of overlapping information. In contrast, our approach consolidates multiple low-quality images into a single high-quality output, preserving information integrity while avoiding redundant storage and transmission. This naturally leads to a degree of data compression. Assuming each pixel in every channel occupies one unit of storage space, let  $N$  denote the number of locations. Then the input data size is  $D_{\text{in}} = N \times (k \cdot H \cdot W \cdot C + \gamma H \cdot \gamma W \cdot 1)$ , and the output data size is  $D_{\text{out}} = N \times (\gamma H \cdot \gamma W \cdot C)$ . While redundancy reduction is guaranteed, the total physical data volume depends on specific conditions. Because the fused output typically has higher spatial resolution and more channels, the enhanced information richness may increase total data size. Only when  $k$  is sufficiently large

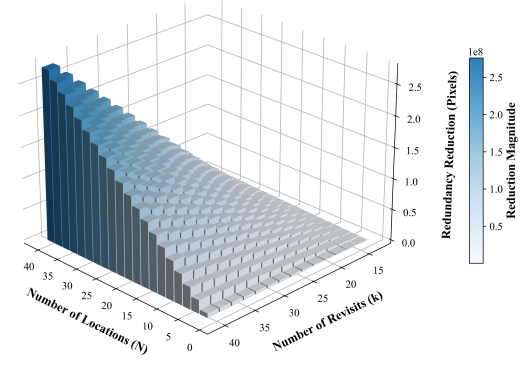


Fig. 12: Difference in data volume between input and output images ( $D_{\text{in}} - D_{\text{out}}$ ,  $H(W) = 256$ ,  $C = 4$ ,  $\gamma = 4$ )

does the compression benefit outweigh this increase, satisfying  $D_{\text{out}} < D_{\text{in}}$ . As shown in Fig. 12, this advantage becomes increasingly pronounced in Sat-IoT scenarios characterized by abundant multi-frame data.

## 7 Conclusion

In this paper, we propose *SatFusion*, an end-to-end unified framework that jointly exploits multi-frame and multi-source RS images to overcome the limitations caused by task separation in existing MFSR and pansharpening methods, while maintaining strong extensibility for integrating existing networks. *SatFusion* demonstrates stable performance under challenging conditions such as image blur and large modality gaps. Furthermore, we introduce *SatFusion\** to further enhance model quality and generalization. Extensive experiments on the WorldStrat, WV3, GF, and QB datasets show that *SatFusion* and *SatFusion\** significantly outperform existing methods by effectively leveraging complementary information across multi-frame and multi-source data, validating their effectiveness and practical value in complex RS scenarios.

Nevertheless, performance may degrade under extreme geometric misalignment, strong temporal dynamics, or severe cross-sensor spectral response discrepancies. Future work will explore more faithful sensor-aware degradation models, broader cross-domain generalization, and more efficient inference that scales gracefully with the number of input frames.

**Acknowledgements** This work was supported in part by NSFC grant (62502446, 62125206), in part by the Ningbo Yongjiang Talent Programme Grant 2024A-402-G and in part by the fund of Oak Grove Ventures-School of Software Technology, Zhejiang University Blockchain Joint Lab. The datasets supporting the findings of this study are publicly available at the following URL: <https://github.com/liangjiandeng/PanCollection.git>,

<https://doi.org/10.5281/zenodo.6810792>. All trained models and codes are publicly available on GitHub: <https://github.com/dllgyufei/SatFusion.git>.

## References

1. Alparone, L., Wald, L., Chanussot, J., Thomas, C., Gamba, P., Bruce, L.M.: Comparison of pansharpening algorithms: Outcome of the 2006 grs-s data-fusion contest. *IEEE Transactions on Geoscience and Remote Sensing* **45**(10), 3012–3021 (2007)
2. An, T., Zhang, X., Huo, C., Xue, B., Wang, L., Pan, C.: Tr-misr: Multiimage super-resolution based on feature fusion with transformers. *IEEE Journal of Selected Topics in Applied Earth Observations and Remote Sensing* **15**, 1373–1388 (2022)
3. Bhat, G., Danelljan, M., Van Gool, L., Timofte, R.: Deep burst super-resolution. In: Proceedings of the IEEE/CVF conference on computer vision and pattern recognition, pp. 9209–9218 (2021)
4. Cornebise, J., Oršolić, I., Kalaitzis, F.: Open high-resolution satellite imagery: The worldstrat dataset—with application to super-resolution. *Advances in Neural Information Processing Systems* **35**, 25,979–25,991 (2022)
5. Deng, L.J., Vivone, G., Jin, C., Chanussot, J.: Detail injection-based deep convolutional neural networks for pansharpening. *IEEE Transactions on Geoscience and Remote Sensing* **59**(8), 6995–7010 (2020)
6. Deng, L.J., Vivone, G., Paoletti, M.E., Scarpa, G., He, J., Zhang, Y., Chanussot, J., Plaza, A.: Machine learning in pansharpening: A benchmark, from shallow to deep networks. *IEEE Geoscience and Remote Sensing Magazine* **10**(3), 279–315 (2022)
7. Deudon, M., Kalaitzis, A., Goytom, I., Arefin, M.R., Lin, Z., Sankaran, K., Michalski, V., Kahou, S.E., Cornebise, J., Bengio, Y.: Highres-net: Recursive fusion for multi-frame super-resolution of satellite imagery. *arXiv preprint arXiv:2002.06460* (2020)
8. Di, X., Peng, L., Xia, P., Li, W., Pei, R., Cao, Y., Wang, Y., Zha, Z.J.: Qmambabsr: Burst image super-resolution with query state space model. In: Proceedings of the Computer Vision and Pattern Recognition Conference, pp. 23,080–23,090 (2025)
9. Do, J., Kim, S., Youk, G., Lee, J., Kim, M.: Pan-crafter: Learning modality-consistent alignment for pan-sharpening. *arXiv preprint arXiv:2505.23367* (2025)
10. Do, J., Lee, J., Kim, M.: C-diffset: Leveraging latent diffusion for sar-to-eo image translation with confidence-guided reliable object generation. *arXiv preprint arXiv:2411.10788* (2024)
11. Dosovitskiy, A.: An image is worth 16x16 words: Transformers for image recognition at scale. *arXiv preprint arXiv:2010.11929* (2020)
12. Duan, Y., Wu, X., Deng, H., Deng, L.J.: Content-adaptive non-local convolution for remote sensing pansharpening. In: Proceedings of the IEEE/CVF Conference on Computer Vision and Pattern Recognition, pp. 27,738–27,747 (2024)
13. He, K., Chen, X., Xie, S., Li, Y., Dollár, P., Girshick, R.: Masked autoencoders are scalable vision learners. In: Proceedings of the IEEE/CVF conference on computer vision and pattern recognition, pp. 16,000–16,009 (2022)
14. He, L., Rao, Y., Li, J., Chanussot, J., Plaza, A., Zhu, J., Li, B.: Pansharpening via detail injection based convolutional neural networks. *IEEE Journal of Selected Topics in Applied Earth Observations and Remote Sensing* **12**(4), 1188–1204 (2019)
15. He, X., Cao, K., Zhang, J., Yan, K., Wang, Y., Li, R., Xie, C., Hong, D., Zhou, M.: Pan-mamba: Effective pan-sharpening with state space model. *Information Fusion* **115**, 102,779 (2025)
16. He, X., Yan, K., Zhang, J., Li, R., Xie, C., Zhou, M., Hong, D.: Multiscale dual-domain guidance network for pan-sharpening. *IEEE Transactions on Geoscience and Remote Sensing* **61**, 1–13 (2023)
17. Huang, J., Chen, H., Ren, J., Peng, S., Deng, L.: A general adaptive dual-level weighting mechanism for remote sensing pansharpening. In: Proceedings of the Computer Vision and Pattern Recognition Conference, pp. 7447–7456 (2025)
18. Jin, Z.R., Zhang, T.J., Jiang, T.X., Vivone, G., Deng, L.J.: Lagconv: Local-context adaptive convolution kernels with global harmonic bias for pansharpening. In: Proceedings of the AAAI conference on artificial intelligence, vol. 36, pp. 1113–1121 (2022)
19. Kim, S., Do, J., Lee, J., Kim, M.: U-know-diffpan: An uncertainty-aware knowledge distillation diffusion framework with details enhancement for pan-sharpening. In: Proceedings of the Computer Vision and Pattern Recognition Conference, pp. 23,069–23,079 (2025)
20. Kim, T., Kwak, J., Choi, J.P.: Satellite edge computing architecture and network slice scheduling for iot support. *IEEE Internet of Things journal* **9**(16), 14,938–14,951 (2021)
21. Kothari, V., Liberis, E., Lane, N.D.: The final frontier: Deep learning in space. In: Proceedings of the 21st international workshop on mobile computing systems and applications, pp. 45–49 (2020)
22. Li, J., Li, D., Xiong, C., Hoi, S.: Blip: Bootstrapping language-image pre-training for unified vision-language understanding and generation. In: International conference on machine learning, pp. 12,888–12,900. PMLR (2022)
23. Li, J., Pei, Y., Zhao, S., Xiao, R., Sang, X., Zhang, C.: A review of remote sensing for environmental monitoring in china. *Remote Sensing* **12**(7), 1130 (2020)
24. Li, Y., Zhang, L., Dingl, C., Wei, W., Zhang, Y.: Single hyperspectral image super-resolution with grouped deep recursive residual network. In: 2018 IEEE Fourth International Conference on Multimedia Big Data (BigMM), pp. 1–4. IEEE (2018)
25. Liu, Z., Hu, H., Lin, Y., Yao, Z., Xie, Z., Wei, Y., Ning, J., Cao, Y., Zhang, Z., Dong, L., et al.: Swin transformer v2: Scaling up capacity and resolution. In: Proceedings of the IEEE/CVF conference on computer vision and pattern recognition, pp. 12,009–12,019 (2022)
26. Liu, Z., Lin, Y., Cao, Y., Hu, H., Wei, Y., Zhang, Z., Lin, S., Guo, B.: Swin transformer: Hierarchical vision transformer using shifted windows. In: Proceedings of the IEEE/CVF international conference on computer vision, pp. 10,012–10,022 (2021)
27. Lofqvist, M., Cano, J.: Accelerating deep learning applications in space. *arXiv preprint arXiv:2007.11089* (2020)
28. Loncan, L., De Almeida, L.B., Bioucas-Dias, J.M., Briottet, X., Chanussot, J., Dobigeon, N., Fabre, S., Liao, W., Licciardi, G.A., Simoes, M., et al.: Hyperspectral pansharpening: A review. *IEEE Geoscience and remote sensing magazine* **3**(3), 27–46 (2015)
29. Loshchilov, I., Hutter, F.: Sgdr: Stochastic gradient descent with warm restarts. *arXiv preprint arXiv:1608.03983* (2016)
30. Masi, G., Cozzolino, D., Verdoliva, L., Scarpa, G.: Pansharpening by convolutional neural networks. *Remote Sensing* **8**(7), 594 (2016)
31. Meng, Q., Shi, W., Li, S., Zhang, L.: Pandiff: A novel pansharpening method based on denoising diffusion probabilistic model. *IEEE Transactions on Geoscience and Remote Sensing* **61**, 1–17 (2023)

32. Meng, X., Xiong, Y., Shao, F., Shen, H., Sun, W., Yang, G., Yuan, Q., Fu, R., Zhang, H.: A large-scale benchmark data set for evaluating pansharpening performance: Overview and implementation. *IEEE Geoscience and Remote Sensing Magazine* **9**(1), 18–52 (2020)

33. Molini, A.B., Valsesia, D., Fracastoro, G., Magli, E.: Deepsum: Deep neural network for super-resolution of unregistered multitemporal images. *IEEE Transactions on Geoscience and Remote Sensing* **58**(5), 3644–3656 (2019)

34. Neyns, R., Canters, F.: Mapping of urban vegetation with high-resolution remote sensing: A review. *Remote sensing* **14**(4), 1031 (2022)

35. Peng, S., Guo, C., Wu, X., Deng, L.J.: U2net: A general framework with spatial-spectral-integrated double u-net for image fusion. In: Proceedings of the 31st ACM International Conference on Multimedia, pp. 3219–3227 (2023)

36. Pohl, C., Van Genderen, J.L.: Review article multisensor image fusion in remote sensing: concepts, methods and applications. *International journal of remote sensing* **19**(5), 823–854 (1998)

37. Razzak, M.T., Mateo-Garcia, G., Lecuyer, G., Gómez-Chova, L., Gal, Y., Kalaitzis, F.: Multi-spectral multi-image super-resolution of sentinel-2 with radiometric consistency losses and its effect on building delineation. *ISPRS Journal of Photogrammetry and Remote Sensing* **195**, 1–13 (2023)

38. Salvetti, F., Mazzia, V., Khalil, A., Chiaberge, M.: Multi-image super resolution of remotely sensed images using residual attention deep neural networks. *Remote Sensing* **12**(14), 2207 (2020)

39. Shi, W., Caballero, J., Huszár, F., Totz, J., Aitken, A.P., Bishop, R., Rueckert, D., Wang, Z.: Real-time single image and video super-resolution using an efficient sub-pixel convolutional neural network. In: Proceedings of the IEEE conference on computer vision and pattern recognition, pp. 1874–1883 (2016)

40. Thomas, C., Ranchin, T., Wald, L., Chanussot, J.: Synthesis of multispectral images to high spatial resolution: A critical review of fusion methods based on remote sensing physics. *IEEE Transactions on Geoscience and Remote Sensing* **46**(5), 1301–1312 (2008)

41. Vaswani, A., Shazeer, N., Parmar, N., Uszkoreit, J., Jones, L., Gomez, A.N., Kaiser, L., Polosukhin, I.: Attention is all you need. *Advances in neural information processing systems* **30** (2017)

42. Vivone, G., Dalla Mura, M., Garzelli, A., Restaino, R., Scarpa, G., Ulfarsson, M.O., Alparone, L., Chanussot, J.: A new benchmark based on recent advances in multispectral pansharpening: Revisiting pansharpening with classical and emerging pansharpening methods. *IEEE Geoscience and Remote Sensing Magazine* **9**(1), 53–81 (2020)

43. Wald, L., Ranchin, T., Mangolini, M.: Fusion of satellite images of different spatial resolutions: Assessing the quality of resulting images. *Photogrammetric engineering and remote sensing* **63**(6), 691–699 (1997)

44. Wang, S., Li, Q.: Satellite computing: Vision and challenges. *IEEE Internet of Things Journal* **10**(24), 22,514–22,529 (2023)

45. Wang, X., Zheng, Z., Shao, J., Duan, Y., Deng, L.J.: Adaptive rectangular convolution for remote sensing pansharpening. In: Proceedings of the Computer Vision and Pattern Recognition Conference, pp. 17,872–17,881 (2025)

46. Wang, Y., He, X., Wu, C., Huang, J., Zhang, S., Liu, R., Ding, X., Che, H.: Mmmamba: A versatile cross-modal in context fusion framework for pan-sharpening and zero-shot image enhancement. *arXiv preprint arXiv:2512.15261* (2025)

47. Wang, Z., Bovik, A.C., Sheikh, H.R., Simoncelli, E.P.: Image quality assessment: from error visibility to structural similarity. *IEEE transactions on image processing* **13**(4), 600–612 (2004)

48. Wei, P., Sun, Y., Guo, X., Liu, C., Li, G., Chen, J., Ji, X., Lin, L.: Towards real-world burst image super-resolution: Benchmark and method. In: Proceedings of the IEEE/CVF International Conference on Computer Vision, pp. 13,233–13,242 (2023)

49. Wei, Y., Yuan, Q., Shen, H., Zhang, L.: Boosting the accuracy of multispectral image pansharpening by learning a deep residual network. *IEEE Geoscience and Remote Sensing Letters* **14**(10), 1795–1799 (2017)

50. Wellmann, T., Lausch, A., Andersson, E., Knapp, S., Cortinovis, C., Jache, J., Scheuer, S., Kremer, P., Mascarenhas, A., Kraemer, R., et al.: Remote sensing in urban planning: Contributions towards ecologically sound policies? *Landscape and urban planning* **204**, 103,921 (2020)

51. Xing, Y., Qu, L., Zhang, S., Feng, J., Zhang, X., Zhang, Y.: Empower generalizability for pansharpening through text-modulated diffusion model. *IEEE Transactions on Geoscience and Remote Sensing* (2024)

52. Xing, Y., Qu, L., Zhang, S., Xu, D., Yang, Y., Zhang, Y.: Dual-granularity semantic guided sparse routing diffusion model for general pansharpening. In: Proceedings of the Computer Vision and Pattern Recognition Conference, pp. 12,658–12,668 (2025)

53. Xu, Y., Bai, T., Yu, W., Chang, S., Atkinson, P.M., Ghamisi, P.: Ai security for geoscience and remote sensing: Challenges and future trends. *IEEE Geoscience and Remote Sensing Magazine* **11**(2), 60–85 (2023)

54. Yang, J., Fu, X., Hu, Y., Huang, Y., Ding, X., Paisley, J.: Pannet: A deep network architecture for pan-sharpening. In: Proceedings of the IEEE international conference on computer vision, pp. 5449–5457 (2017)

55. Yang, J., Gong, P., Fu, R., Zhang, M., Chen, J., Liang, S., Xu, B., Shi, J., Dickinson, R.: The role of satellite remote sensing in climate change studies. *Nature climate change* **3**(10), 875–883 (2013)

56. Yuan, Q., Shen, H., Li, T., Li, Z., Li, S., Jiang, Y., Xu, H., Tan, W., Yang, Q., Wang, J., et al.: Deep learning in environmental remote sensing: Achievements and challenges. *Remote sensing of Environment* **241**, 111,716 (2020)

57. Yuan, Q., Wei, Y., Meng, X., Shen, H., Zhang, L.: A multi-scale and multidepth convolutional neural network for remote sensing imagery pan-sharpening. *IEEE Journal of Selected Topics in Applied Earth Observations and Remote Sensing* **11**(3), 978–989 (2018)

58. Yuhas, R.H., Goetz, A.F., Boardman, J.W.: Discrimination among semi-arid landscape endmembers using the spectral angle mapper (sam) algorithm. In: JPL, Summaries of the Third Annual JPL Airborne Geoscience Workshop. Volume 1: AVIRIS Workshop (1992)

59. Zhong, Y., Wu, X., Cao, Z., Dou, H.X., Deng, L.J.: Ssdif: Spatial-spectral integrated diffusion model for remote sensing pansharpening. *Advances in Neural Information Processing Systems* **37**, 77,962–77,986 (2024)

60. Zhu, Z., Cao, X., Zhou, M., Huang, J., Meng, D.: Probability-based global cross-modal upsampling for pansharpening. In: Proceedings of the IEEE/CVF Conference on Computer Vision and Pattern Recognition, pp. 14,039–14,048 (2023)